SIMULATION OF ANISOTROPIC WAVE PROPAGATION IN VERTICAL SEISMIC PROFILES

A Thesis

by

VINCENT BERNARD DURUSSEL

Submitted to the Office of Graduate Studies of
Texas A&M University
in partial fulfillment of the requirements for the degree of

MASTER OF SCIENCE

August 2002

Major Subject: Geophysics

SIMULATION OF ANISOTROPIC WAVE PROPAGATION IN VERTICAL SEISMIC PROFILES

A Thesis

by

VINCENT BERNARD DURUSSEL

Submitted to the Office of Graduate Studies of
Texas A&M University
In partial fulfillment of the requirements for the degree of

MASTER OF SCIENCE

Approved as to style and format by:

Richard L. Gibson
(Chair of Committee)

Mark Everett
(Member)

Thomas Blasingame
(Member)

Andrew Hajash
(Head of Department)

August 2002

Major Subject: Geophysics

ABSTRACT

Simulation of Anisotropic Wave Propagation
in Vertical Seismic Profiles. (August 2002)
Vincent Bernard Durussel, M.Eng., UPMC, Paris, France;
Chair of Advisory Committee: Dr Richard Gibson

The influence of elastic anisotropy on seismic wave propagation is often neglected for the sake of simplicity. However, ignoring anisotropy may lead to significant errors in the processing of seismic data and ultimately in a poor image of the subsurface. This is especially true in wide-aperture Vertical Seismic Profiles where waves travel both vertically and horizontally. Anisotropy has been neglected in wavefront construction methods of seismic ray-tracing until Gibson (2000), who showed they are powerful tools to simulate seismic wave propagation in three-dimensional anisotropic subsurface models. The code is currently under development using a C++ object oriented programming approach because it provides high flexibility in the design of new components and facilitates debugging and maintenance of a complex algorithm. So far, the code was used to simulate propagation in homogeneous or simple heterogeneous anisotropic velocity models mainly designed for testing purposes. In particular, it has never been applied to simulate a field dataset. We propose here an analytical method involving little algebra and that allows the design of realistic heterogeneous anisotropic models using the C++ object oriented programming approach. The new model class can model smooth multi-layered subsurface with gradients or models with many dip variations. It has been used to model first arrival times of a wide-aperture VSP dataset from the Gulf of Mexico to estimate the amount of anisotropy. The proposed velocity model is transversely isotropic. The anisotropy is constant throughout the model and is defined via Thomsen's parameters. Values in the final model are $e = 0.055$ and $d = -0.115$. The model is compatible with the a priori knowledge of the local geology and reduces the RMS average time difference between measured and computed travel times by 51% in comparison to the initial isotropic model. These values are realistic and are similar to other measurements of anisotropy in the Gulf of Mexico.

To Mother in Memoriam

ACKNOWLEDGMENTS

I would like to thank Dr Richard Gibson, the chairman of my committee, for giving me the opportunity to work with him (I only thought I knew what scientific rigor was!). I would also like to thank Dr Mark Everett and Dr Thomas Blasingame, who accepted to be members of my committee. I am also grateful to Dr Gibson's student team: Jin Lee, Costa, John Priest, Sung Yuh and the others for their patience and their help. This project was also a collaborative effort between the Geosciences and the Computer Sciences Departments and I thank Dr Nancy Amato and her students (Derek and Paul) for their help and their useful advice during the monthly meetings. This Master is a joint program between Texas A&M and the French Petroleum Institute (IFP) and I would like to thank Mr Alain Auriault and all the IFP members who made this program possible. I was sponsored by Total-Final-Elf and I am very grateful to them for their financial support. I am also grateful to Paul Constance and Steve Roche (from OPEX) who provided the VSP dataset. This research was supported by the National Science Foundation under grant number ACI-0081510.

I would like to make a special thanks to my sister Marie-Claire and my father Jean-Jacques and more generally to my whole family. They are always on my side no matter the choices that I make or the distance that lies between us.

I also would like to thank Matthieu Plantevin, who has been my roommate, carmate and my friend throughout this Master program as well as Clement Mialet who welcomed me in College Station whenever I was homeless.

Special thanks to my favorite CD, for her true love and support (do I really deserve this?).

TABLE OF CONTENTS

Page

LIST OF FIGURES

LIST OF TABLES

CHAPTER I

INTRODUCTION

An elastic medium is said to be anisotropic when its physical properties at a given location depend on the direction in which they are considered (Wetzel, 1987). The potential anisotropic behavior of seismic waves in oil exploration has often been neglected for the sake of simplicity. However, as the accuracy and the complexity offered by modern technology increases, such a phenomenon must be taken into account. Indeed, in wide-aperture walkaway vertical seismic profiles or in long offset surface seismic surveys, waves do not only travel vertically. In such cases, ignoring anisotropy may lead to significant errors in velocity analysis, normal moveout (NMO), dip moveout (DMO), migration, time-to-depth conversion, and Amplitude Versus Offset (AVO) analysis. Ultimately, this may lead to a poor localization of the target. In addition to this, some phenomena observed in the earth subsurface, such as the splitting of shear-waves according to their direction of polarization (Godfrey et al., 2000; Kay et al., 1999; Papadimitriou et al., 1999; Plenefish et al., 2001; among others) have only been explained by the theory of anisotropy.

An increasing effort has been made to estimate the influence of anisotropy on seismic dataset (Alford et al., 1989; Hilterman et al, 1998; Raymer et al., 1999; Shuck, 1991; Sriram et al., 1983; Thomsen, 1986; Wetzel, 1987; among others) and it appears that the anisotropic behavior of subsurface layers may not be negligible. For instance, Sriram et al. (1983) evaluated the SV-wave anisotropy in a field in southeast Texas (USA). They simply calculated the ratio of the horizontal velocity estimated with far-offset reflection NMO velocities and the vertical velocity measured with a zero-offset VSP. They found that the average ratio was 1.4. In this particular case neglecting the anisotropic behavior of the subsurface may have led to a 40% error in the velocity analysis.

Dataset and objectives

In this project, we propose to evaluate the amount of anisotropy in a seismic dataset

---

This thesis follows the style and format of Geophysics.

acquired over a mature onshore field in the South Louisiana Salt Basin, Gulf of Mexico. The three dimensional surface seismic survey was acquired at the same time as wide-aperture three-dimensional, three-component vertical seismic profiles (Constance et al., 1999). The main geological feature of the subsurface is a salt dome that has pierced the overlying sediments. A synthetic three-dimensional isotropic velocity model has been determined by velocity analysis on the surface seismic data (Priest, personal communication). In parallel, a one-dimensional velocity model has been calculated using the nearest offset vertical seismic profile (Tzimeas, personal communication). The latter has been used to calibrate a two-dimensional isotropic model to compute synthetic arrival times on a chosen profile. As a result, comparison of the computed arrival times with the measured ones exhibited a good match for near offset, but large errors as offset increases. We attempt here to find an anisotropic velocity model that fully explains the far offset first arrival times as well as the near offset ones. As a comparison an isotropic solution is also proposed to reduce the far offset errors.

The tool

Different numerical methods are available to simulate seismic wave propagation in the earth subsurface. However, inverting a field dataset by considering complex velocity models requires a large amount of computations. Among all of the techniques involving small calculation times, ray methods are the most interesting because they compute all the information required for subsequent applications, i.e. travel times, amplitudes and displacement vectors (Babich, 1961; Cervený, 1972; Cervený, 2001). Other techniques such as finite differences of the eikonal equation compute travel times rapidly and accurately, but may lead to unreliable amplitude computations (Vidale, 1990; Van Trier and Symes, 1991; Moser, 1991; Zhang and Toksöz, 1998).

Ray methods are based on a high-frequency approximation of the wave equation (Gibson et al., 1991; Cervený, 2001). A ray is the individual travel path of an infinitely small portion of the wave energy from the source to the receiver. According to Fermat's principle, this path is stationary as long as the properties of the medium do not change with time. Once the path is found, the solution provides the information we want all along the ray, but only along the ray. Therefore, classical methods (such as ray-shooting or ray-bending methods) use an iterative process to find the ray exactly connecting a source to a receiver. This can be time consuming, especially when measurements for a great number of source-receiver pairs must be simulated. Methods using a paraxial approximation, such as wavefront construction methods avoid this iterative process by extrapolating the information computed at the ray to its vicinity (Gibson, 2000; Lambaré, 1996; Vinje, 1993). A fan of rays can then be propagated from the source with a density sufficient to allow accurate extrapolations anywhere within the bounding box of the model. Another strength of wavefront construction methods is that they optimize the density of rays by interpolating new rays at some distance from the source when required. However, so far, these methods have ignored an important aspect of seismic wave propagation, which is velocity anisotropy (Gibson, 2000). To be complete and efficient, wavefront construction methods must take this potential aspect of wave propagation into account. The algorithm developed by Gibson (2000) can include arbitrary types of anisotropy. The computation of the ray field starts by the calculation of a sparse number of rays initially propagating from the source toward a predefined set of directions. A time step interval is given for the computation of wavefronts. The latter are simply built by linking neighboring ray points at the time of interest. As a result, wavefronts are made of quadrilateral surface elements in the three-dimensional space. At each time step, each element is tested to see if the density of ray throughout the model is high enough to maintain the desired accuracy. If not, new rays are interpolated using a paraxial approximation (Gibson et al., 1991). Once the ray field computation is done, travel time and amplitude information may be extrapolated at receiver locations using the same method.

The algorithm by wavefront construction is being developed with a C++ object oriented programming approach. This language provides a great flexibility in the development of new components by allowing the programmer to create unique data types as well as the procedures to manipulate them (Stroustrup, 1997; Schildt, 1998; Stevens and Walnum, 2000). In contrast, to classical programming approach (procedural programming), the data structure and its related functions are encapsulated altogether under a new type of variable named *object*. The abstract declaration of the new object type (including its procedures) is called a *class*. Subsequent developments are facilitated by the design of new object classes derived from the previous ones and adding their own specificities. Procedures common to all different types of variables (including the future ones) can be declared at once under generic object types named *templates*.

Then, if properly coded, the previous components of the algorithm do not have to be modified each time a new functionality is added.

Overview and method

This approach will allow us to use the components of the algorithm already developed to simulate new types of earth models. Indeed, so far the algorithm has been used with homogeneous models and with simple heterogeneous models (e.g. a high velocity region modeled by a Gaussian) mainly designed for testing purposes. Furthermore, it has never been used to invert real data. The first part of this project is to develop realistic heterogeneous anisotropic models using the C++ object oriented programming approach. In other words, the anisotropic model objects previously implemented must be extended to allow the software to build synthetic dataset that can be compared to real dataset. This can be done effectively by simply modeling the main geological structures usually encountered in the earth subsurface. Models can be expressed analytically to allow a simple coding and not increase computation time significantly. The simplest assumption on the heterogeneity of the subsurface usually considered is a vertical velocity gradient (Popov and Camerlynck, 1996; Miller at al., 1997; Julia et al., 1998; Mitchell, 1998; Bostock, 1999; Hansen et al., 1999; Muller et al., 2000; Tittgemeyer et al., 2000; Darbyshire et al., 2000; Mereu, 2000; Wang et al., 2000; Dean et al., 2000; among others). Heterogeneous anisotropic earth model classes containing gradients can be implemented with little algebra. Once it is shown that the new models can satisfactorily simulate some simple, but realistic subsurface structures (e.g. layers, syncline, anticline, etc), they will be used in the second part of the project: the search of an anisotropic model that reduces the far-offset discrepancies between computed and measured first arrival times for the studied dataset.

This report begins with a review of the basic principles of ray tracing in anisotropic media and a detailed description of the algorithm. Then the methodology to implement realistic gradient models using a C++ object oriented programming approach is given. The next part summarizes field measurements that have been done on seismic anisotropy, especially in the Gulf of Mexico. This knowledge will help us to develop realistic models. In a last part we present the dataset, the synthetic models that have been considered and the results.

CHAPTER II

RAY TRACING IN ANISOTROPIC MEDIA

Ray methods were first applied to anisotropic media by Babich (1961) and then reworked by Cervený (1972). More recently, Cervený (2001) presented a more complete review of ray-tracing theory in inhomogeneous anisotropic media. The purpose of the ray-tracing methods is to rapidly compute an approximate solution to the wave equation. The basic results compute travel path, travel time, amplitude and displacement vector of the seismic wave, given an initial direction and amplitude of the energy flux. The individual travel path of an infinitely small part of the seismic wave energy flux is simply called a ray. Ray methods are based on a high-frequency asymptotic solution of the wave equation (Gibson et al., 1991). The main assumption implied by those methods is that the characteristic length of the medium must be larger than the wavelength of the propagating signal. In other words, the medium can only be "smoothly inhomogeneous" and its physical properties cannot vary greatly within a wavelength. This approximation allows us to retain only two terms in the development of the wave equation: the first term leads to ray-path and travel time, and the second term to the amplitude of the seismic wave. Because we only use travel times in this project, we will only expose the basic theory directly related to the first term.

Linear elastodynamics

Even though the basic concepts and equations of linear elastodynamics have been explained in many textbooks and papers (Aki and Richards, 1980; Cervený 1972; Cervený, 2001; among others), we shall make a short review to help the reader to understand how rays are computed. This introduction essentially follows the theoretical developments and notations proposed by Cervený (2001). However, only the final, most important formulae are presented without derivation.

Hooke's law gives the relationship between stress and strain in a perfectly elastic solid (Aki and Richard, 1980; Cervený, 2001):

$$t_{ij} = c_{ijkl} e_{kl} , \tag{2-1}$$

where c_{ijkl} are the components of the elastic tensor, and t_{ij} and e_{kl} are the stress and the strain tensors, respectively, expressed in Cartesian coordinates. The elastic tensor c_{ijkl} contains all the relevant information regarding the elastic properties of the medium, even for arbitrary anisotropy. The total number of coefficients is $3^4 = 81$, but some of them are equal. The number of independent components is determined by the following symmetry relationships:

$$c_{ijkl} = c_{jikl} = c_{ijlk} = c_{klij}. \qquad (2\text{-}2)$$

As a result, the elastic tensor has only 21 independent components for a medium of arbitrary anisotropy. For this reason, the components of the elastic tensor c_{ijkl} are often expressed in abbreviated Voigt form, where the 3 x 3 x 3 x 3 tensor is replaced by a 6 x 6 matrix whose components are often denoted by capital letters C_{mn}. The first index m pertains to pair of former indices i,j and index n to pair k,l in the following manner (Cervený, 2001): 1 ->1,1; 2 -> 2,2; 3 -> 3,3; 4 -> 2,3; 5 -> 1,3; 6 -> 1,2; for both new indices m and n. For instance, with this notation $c_{1122} = C_{12}$. As a result, the matrix C_{mn} is also symmetric:

$$C = \begin{pmatrix} C_{11} & C_{12} & C_{13} & C_{14} & C_{15} & C_{16} \\ & C_{22} & C_{23} & C_{24} & C_{25} & C_{26} \\ & & C_{33} & C_{34} & C_{35} & C_{36} \\ & & & C_{44} & C_{45} & C_{46} \\ & \dots & & & C_{55} & C_{56} \\ & & & & & C_{66} \end{pmatrix}. \qquad (2\text{-}3)$$

We shall use the Voigt notation later in this report to describe various symmetries in anisotropic media or even to quantify the amount of anisotropy.

The elastodynamic equation for an elastic medium is given by (Aki and Richard, 1980; Cervený, 2001):

$$\left(c_{ijkl}u_{k,l}\right)_{,j} + f_i = r\ddot{u}_i , \qquad (2\text{-}4)$$

where u_k are the Cartesian components of the displacement vector, f_i is a source term (body forces) and r the density of the medium. Here a comma in front of subscripts indicates differentiation with respect to space coordinates, a dot on a top of a quantity indicates differentiation with respect to time and the Einstein summation is applied. The elastodynamic equation (2-4) represents a system of three partial differential equations governing the motion of an infinitely small portion of elastic material. Its solution allows us to simulate the behavior of the elastic medium when an external energy source (such as a shock or more generally a force) is applied to it and to understand ground motions recorded when waves propagate. However, for complex media, the derivation of a solution for system (2-4) can become very difficult and we seek a simplified form for displacement $\vec{u}$ by using a high frequency approximation (after Cervený, 2001):

$$u_i\left(x_j, t\right) = U_i\left(x_j\right) F\left(t - T\left(x_j\right)\right), \tag{2-5}$$

where *F(t)* is a propagating signal varying rapidly with t and $\vec{U}\left(\vec{x}\right)$ is in general a complex-valued vectorial function independent of the time. $T\left(\vec{x}\right)$ is simply a scalar function of the Cartesian coordinates and it has a dimension of a time. *F(t)* is called the "high frequency analytical signal" (Cervený, 2001) because its Fourier transform (giving the signal spectrum in the frequency domain) vanishes for low frequency. $T\left(\vec{x}\right)$ is usually called the phase function. To intuitively understand its role in equation (2-5) let us consider the simpler case of a plane wave. In this approach, the propagating wavefront is a plane of constant phase and function $T\left(\vec{x}\right)$ is given by the equation of a plane in the three-dimensional space: $T\left(\vec{x}\right) = \vec{p} \cdot \vec{x}$. The vector $\vec{p}$ is normal to the plane and gives the direction of propagation of the wavefront as well as its velocity. The norm of the vector $\vec{p}$ is called the phase slowness because it is the reciprocal of the wavefront (phase) velocity. However, the plane wave solution is only valid in homogeneous media (Cervený, 2001). In the more general solution provided by the high frequency approximation, functions $\vec{U}\left(\vec{x}\right)$ and $T\left(\vec{x}\right)$ can vary "arbitrarily (but slowly) with the coordinates" (Cervený, 2001).

Inserting solution (2-5) into the elastodynamic equation (2-4) when $f_i = 0$ and approximating for high frequency (i.e. only considering the first term) leads to the Christoffel equation (Cervený, 2001):

$$\Gamma_{ik} U_k - U_i = \left(\Gamma_{ik} - d_{ik}\right) U_k = 0, \tag{2-6}$$

with $\Gamma_{ik} = a_{ijkl} T_{,j} T_{,l}$, $a_{ijkl} = c_{ijkl} / r$ and $T_{,j} = p_j$. (2-7)

To solve the characteristic equation (2-6) for a non-trivial case (U_k ? 0), we must calculate the eigenvalues of the matrix G also named the Christoffel matrix. The latter is a 3-by-3 matrix leading to three eigenvalues denoted G_m (m=1, 2 or 3) and three eigenvectors $\vec{g}^{(m)}$ for an elastic medium of arbitrary anisotropy. Eigenvalues and eigenvectors provide three different phase slownesses and the corresponding polarization directions, respectively. Therefore, they define three different modes of propagation. Unlike in an isotropic medium, these different seismic body waves do not necessarily travel independently. Hence, directions of polarization are not necessarily longitudinal or transverse. For this reason we use the word ‘quasi’ to qualify the three modes of propagation: quasi-compressional (qP) and quasi-shear (qS1 and qS2). In an isotropic medium, the velocity of shear waves is the same, no matter the direction of polarization, which leads to two modes of body wave propagation (P and S). In other words, the isotropic case can be considered as a degenerate case of anisotropy where the Christoffel matrix (equations 2-7) has only two eigenvalues. In contrast, in an anisotropic medium, since physical properties are direction dependent, the shear wave velocity depends on the direction of polarization leading to a shear wave splitting. Equation 2-7 leads to the ray-tracing system, the solution of which provides ray path and travel time.

Ray tracing system

We consider a purely anisotropic medium without any singularity. In such media, the three eigenvalues of the matrix G_{ik} (equation 2-7) are different. In other words,

$$G_1(x_i, p_i) \neq G_2(x_i, p_i) \neq G_3(x_i, p_i). \qquad \text{(2-8)}$$

Indeed, if two of these eigenvalues are equal, which happens when there is a shear wave singularity (velocity of qS1 equal to velocity of qS2), the two corresponding eigenvectors cannot be determined uniquely. Equation (2-6) is satisfied if, and only if (Cervený, 2001),

$$\det(\Gamma_{ik} - d_{ik}) = 0\,. \qquad \text{(2-9)}$$

Equation (2-9) simply states that one of the three eigenvalues of the matrix G must equal unity:

$$G_m(p_i) = 1\,, \quad \text{m = 1, 2 or 3.} \qquad \text{(2-10)}$$

The above equation is often called the Eikonal equation. This equation describes the propagation of the wavefront where the phase function $T(\vec{x})$ is constant and therefore allows the computation of the phase slowness and travel time. From equation (2-10), the ray-tracing system can be derived using the method of characteristics (Bleistein, 1984; Cervený, 2001):

$$\frac{dx_i}{dT} = a_{ijkl}\, p_l g_j^{(m)} g_k^{(m)}, \tag{2-11a}$$

$$\frac{dp_i}{dT} = -\frac{1}{2}\frac{\partial a_{jknl}}{\partial x_i}\, p_k p_n g_j^{(m)} g_l^{(m)}. \tag{2-11b}$$

The above system of equation is the nucleus of the algorithm described in the next chapter and allows us to compute the travel path and travel time of a ray propagating in a medium of arbitrary anisotropy, given the initial position and direction of the ray (Gajewski and Pšencik, 1987; Gibson, 1991). The initial position $x_i(T_0) = x_{0i}$ indicates the starting point of the ray and is usually taken as the source location, in conventional ray-shooting methods. The density of rays and the directions of interest (matching the position of an array of receivers for example) may define the initial direction $p_i(T_0) = p_{0i}$. To determine the right hand side of the ray tracing system (2-11), we need to know the density-normalized elastic parameters a_{ijkl} and their spatial derivatives (given by the elastic medium where the waves propagate), the components of the slowness vector $\vec{p}$, and the components of eigenvectors $\vec{g}^{(m)}$ (obtained from eigenvalues and eigenvectors of matrix G given by equation 2-7). The system of equations (2-11) can only be solved analytically in some very trivial cases and is usually solved numerically. After integration, it provides the coordinates of the ray (equation 2-11a) and the coordinates of the phase slowness vector (equation 2-11b). Function $T(\vec{x})$ is the curvilinear coordinate defining these quantities along the ray. The ray-tracing system (2 -11) also requires that density normalized coefficients must be differentiable to the first order. They must vary continuously with the spatial coordinates. This condition is obviously fulfilled because the high frequency approximation requires them to vary smoothly with spatial coordinates. Similarly, the second term of the ray series requires the elastic coefficients to be differentiable to the second order (Cervený et al., 1977). System (2-11) only fails where there are shear-wave singularities (Gibson et al., 1991; Cervený, 2001), because in this case eigenvectors of the matrix G cannot be determined uniquely.

The ray-tracing system has been introduced and one can discuss now some basic properties of anisotropic solids. Their behavior differs from the isotropic one and a good understanding is required before working with such media.

Types of anisotropy

The anisotropy is a characteristic of a medium where physical properties at a given location depend in the direction in which they are measured. In contrast, in an isotropic medium, physical properties are the same, no matter in which direction they are considered. The seismic anisotropy is most commonly due to (Alford et al., 1989; Cervený, 2001):

(1) Homogeneous but anisotropic beds where microscopic grains have a preferred orientation, such as shale or salt;

(2) Isotropic beds so thinly layered that a seismic wave with wavelength much longer than the layer thicknesses propagates as if in a homogeneous, anisotropic medium;

(3) Vertical fractures that have a preferred orientation.

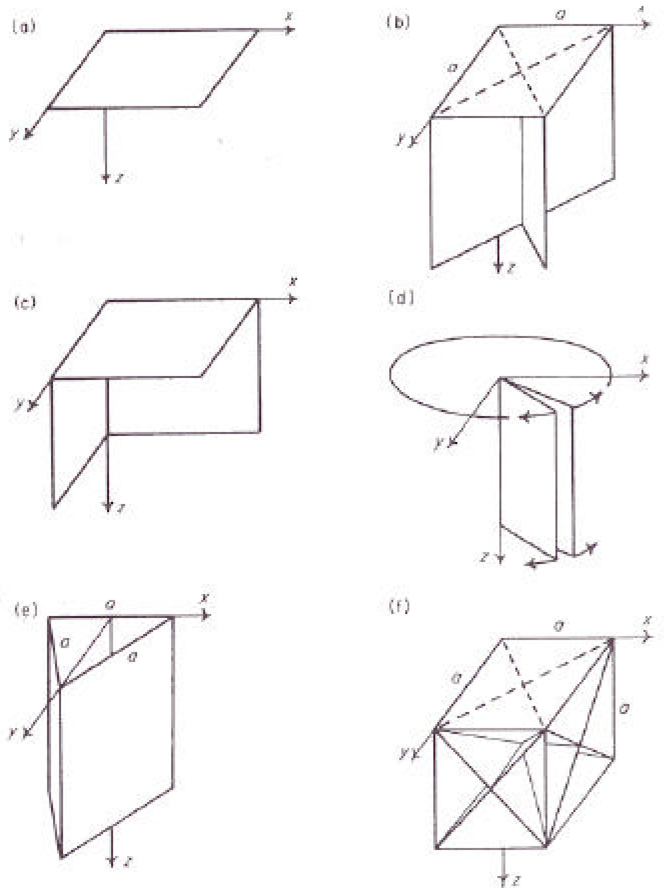

FIG. 2-1. Orientation of symmetry planes of the more common symmetry systems: (a) monoclinic; (b) tetragonal; (c) orthorhombic; (d) hexagonal; (e) trigonal; and (f) cubic (from Crampin, 1984).

There are eight types of anisotropy (Crampin, 1984). Each type of anisotropy presents some symmetry planes with the spatial orientations shown in Figure 2-1 and the corresponding matrices of elastic constants, given in Table 2-1 in Voigt notation (equation 2-3). There are two arrangements of planes mentioned in Table 2-1 but not shown in Figure 2-1. These are the isotropic system with two elastic constants where all planes are symmetry planes and the triclinic system with up to 21 independent elastic constants whose only symmetry is reflection in the origin.

Table 2-1. The range of possible symmetry systems (in Voigt notation, equation 2-3) where *x*, *y*, and *z* are principal axes (from Crampin, 1984). Here, a notation using letters is preferred to notation C_{mn} to ease the visualization of independent components.

Monoclinic

$$\begin{pmatrix} a & b & c & . & . & d \\ b & e & f & . & . & g \\ c & f & h & . & . & i \\ . & . & . & j & k & . \\ . & . & . & k & m & . \\ d & g & i & . & . & n \end{pmatrix}$$

Orthorhombic

$$\begin{pmatrix} a & b & c & . & . & . \\ b & d & e & . & . & . \\ c & e & f & . & . & . \\ . & . & . & g & . & . \\ . & . & . & . & h & . \\ . & . & . & . & . & i \end{pmatrix}$$

Trigonal (x = (a-b)/2)

$$\begin{pmatrix} a & b & c & d & . & . \\ b & a & c & -d & . & . \\ c & c & e & . & . & . \\ d & -d & . & f & . & . \\ . & . & . & . & f & d \\ . & . & . & . & d & x \end{pmatrix}$$

Tetragonal

$$\begin{pmatrix} a & b & c & . & . & . \\ b & a & c & . & . & . \\ c & c & f & . & . & . \\ . & . & . & g & . & . \\ . & . & . & . & h & . \\ . & . & . & . & . & i \end{pmatrix}$$

Hexagonal (x = (a-b)/2)

$$\begin{pmatrix} a & b & c & . & . & . \\ b & a & c & . & . & . \\ c & c & d & . & . & . \\ . & . & . & e & . & . \\ . & . & . & . & e & . \\ . & . & . & . & . & x \end{pmatrix}$$

Cubic

$$\begin{pmatrix} a & b & b & . & . & . \\ b & a & b & . & . & . \\ b & b & a & . & . & . \\ . & . & . & c & . & . \\ . & . & . & . & c & . \\ . & . & . & . & . & c \end{pmatrix}$$

Isotropic

$$\begin{pmatrix} a & b & b & . & . & . \\ b & a & b & . & . & . \\ b & b & a & . & . & . \\ . & . & . & x & . & . \\ . & . & . & . & x & . \\ . & . & . & . & . & x \end{pmatrix}$$

Triclinic

$$\begin{pmatrix} a & b & c & d & e & f \\ b & g & h & i & j & k \\ c & h & l & m & n & o \\ d & i & m & p & q & r \\ e & j & n & q & s & t \\ f & k & o & r & t & u \end{pmatrix}$$

In nature, the most commonly encountered type of anisotropy is hexagonal symmetry (Figure 2-1d and Table 2-1). Such media have one axis of symmetry. Thus, physical properties considered in directions transverse to this symmetry axis are direction independent. For this reason, such media are often said to be transversely isotropic. In what follows, we will mostly consider this type of anisotropy.

Another quantity of primary importance to understand the physical meaning of a ray has not been defined yet: the group velocity.

Group and phase velocity surfaces

The group velocity is the propagation velocity of the energy from the source to the subsurface point of interest. Therefore it is tangent to the ray and it is given by the derivatives of travel path coordinates with respect to the travel time along the ray (equation 2-11a). To help us to understand intuitively the difference between group and phase velocities, Figure 2-2 shows the wavefront at some travel time t for a homogeneous vertical transversely isotropic medium in which the horizontal velocity is greater than the vertical one. For such a medium, the wavefront may have an ellipsoidal shape. In a non-dispersive, homogeneous isotropic medium, group velocity and phase velocity are the same. However, this is not the case in anisotropic media. In Figure 2-2, since the medium is homogeneous, the energy for a given initial direction at the source follows a straight path. On the other hand, the phase velocity gives the velocity of the wavefront and is therefore locally perpendicular to it. Thus, even for a simple case of anisotropy such as transverse isotropy, group velocity and phase velocity both differ in amplitude and direction.

Group and phase velocities are usually visualized using polar surfaces (Cervený, 2001). The phase slowness surface (on the left of Figure 2-3) represents a polar graph of the norm of phase slowness vector as a function of the two take-off angles specifying the direction of the normal to the wavefront. The phase slowness surface is also sometimes simply called the slowness surface. The group velocity surface (on the right of Figure 2-3) represents a polar graph of the norm of the group velocity vector as a function of the two take-off angles specifying the direction of the ray. Because the group velocity is given by the direct path of the energy from the source to the point of interest, the group velocity surface is a wavefront. The wavefront shown in Figure 2-2 is therefore an example of a group velocity surface in a transversely isotropic medium. The group velocity surface is also sometimes called the wave surface.

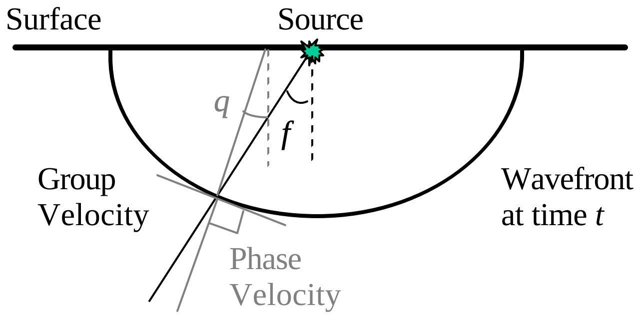

FIG. 2-2. Wavefront in a homogeneous, vertical transversely isotropic medium. Note that phase and group velocities both differ in amplitude and direction. Angles *q* and *f* are respectively the phase (wavefront) and the group (ray) angles (after Thomsen, 1986).

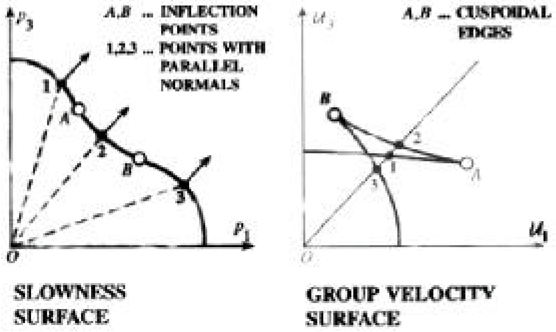

FIG. 2-3. Example of slowness surface (left) and group velocity surface (right) for a shear-wave propagating in a transversely isotropic medium (from Cervený, 2001).

In an isotropic homogeneous medium, all these surfaces are spherical since velocity does not depend on the direction. However, this is not the case for anisotropic homogeneous media (Crampin, 1981). An important property of these surfaces is that the normal to the slowness surface determines the direction to the corresponding group velocity vector. The reciprocal property is also true: the group velocity vector has the same direction as the corresponding normal to the slowness surface. Figure 2-3 shows an example of slowness and group velocity surfaces for a quasi-shear mode propagating in a transversely isotropic medium (Cervený, 2001). The slowness surface on the left side of the figure exhibits a concavity. Therefore, the normal to the slowness surface has the same direction in points 1, 2 and 3. The group velocity surface is then multivalued in the corresponding directions and a triplication in the wavefront exists. Points A and B where the polarity reverses are called cuspoidal points.

Weak elastic anisotropy

In a vertical transversely isotropic medium such as the one shown in Figure 2-2, the amount of anisotropy is usually defined as the ratio between the horizontal and vertical velocities. Thomsen (1986) gathered many field measurements made on transverse isotropy (hexagonal) and concluded that, in most cases, the anisotropy is weak (the ratio is close to one). Thus, he decided to recast equations giving seismic velocities by introducing three parameters defined as (using Voigt notation, equation 2-3):

$$e = \frac{C_{11} - C_{33}}{2C_{33}},$$

$$g = \frac{C_{66} - C_{44}}{2C_{44}}, \qquad (2\text{-}12)$$

and

$$d^* = \frac{1}{2{C_{33}}^2}\left[2\left(C_{13} + C_{44}\right)^2 - \left(C_{33} - C_{44}\right)\left(C_{11} + C_{33} - 2C_{44}\right)\right].$$

The vertical velocities for P- and S-waves are, respectively (Thomsen, 1986):

$$a_0 = \sqrt{C_{33}/r}$$

and (2-13)

$$b_0 = \sqrt{C_{44}/r}\ .$$

A transversely isotropic medium has five independent elastic coefficients (hexagonal symmetry in Table 2-1). The five parameters defined by equations 2-12 and 2-13 can therefore be used to fully recast equations giving the phase velocities of the three modes of propagation:

$$v_p^2(q) = a_0^2\left[1 + e\sin^2 q + D^*(q)\right],$$

$$v_{sv}^2(q) = b_0^2\left[1 + \frac{a_0^2}{b_0^2} e \sin^2 q - \frac{a_0^2}{b_0^2} D^*(q)\right], \tag{2-14}$$

and

$$v_{sh}^2(q) = b_0^2\left[1 + 2g \sin^2 q\right],$$

with

$$D^*(q) = \frac{1}{2}\left(1 - \frac{b_0^2}{a_0^2}\right)\left\{\left[1 + \frac{4d^*}{\left(1 - b_0^2/a_0^2\right)^2}\sin^2 q \cos^2 q + \frac{4\left(1 - b_0^2/a_0^2 + e\right)e}{\left(1 - b_0^2/a_0^2\right)^2}\sin^4 q\right]^{1/2} - 1\right\}. \tag{2-15}$$

Observing that in most cases the three non-dimensional parameters e, g and d are small («1), so that anisotropic velocity values are not far from vertical sound speeds given in (2-13), Thomsen (1986) expanded equation (2-15) in a Taylor series and kept only linear terms in these small parameters:

$$D^*(q) \approx \frac{d^*}{\left(1 - b_0^2/a_0^2\right)}\sin^2 q \cos^2 q + e \sin^4 q\ . \tag{2-16}$$

Using this approximation into equations (2-14) leads to approximated expressions for the phase velocities:

$$\begin{aligned} v_p(q) &= a_0\left(1 + d \sin^2 q \cos^2 q + e \sin^4 q\right), \\ v_{sv}(q) &= b_0\left[1 + \frac{a_0^2}{b_0^2}(e - d)\sin^2 q \cos^2 q\right], \\ v_{sh}(q) &= b_0\left(1 + g \sin^2 q\right), \end{aligned} \tag{2-17}$$

where

$$d = \frac{1}{2}\left[e + \frac{d^*}{\left(1 - b_0^2/a_0^2\right)}\right] = \frac{\left(C_{13} + C_{44}\right)^2 - \left(C_{33} - C_{44}\right)^2}{2C_{33}\left(C_{33} - C_{44}\right)}. \tag{2-18}$$

Expressions (2-17) are only valid for weak anisotropy. Parameters e, g (equations 2-12) and d (equation 2-18) are usually called Thomsen's parameters and are often used in the literature, because they allow a more simple and therefore, more intuitive understanding of transverse isotropy. They also facilitate the quantification of the amount of anisotropy in field measurements. From equations (2-17), it is clear that Thomsen's parameter d will dominate anisotropic effect at near vertical propagation and e will be determinant at horizontal incidence.

Figure 2-4 shows three phase velocity surfaces, when the medium is isotropic and for a vertical transverse isotropic medium with $e = d$ and $e = -d$, respectively. The vertical velocity for the qP mode is 2.35 km/s. Table 2-2 shows the corresponding elastic coefficients in Voigt notation (2-3). Only the five independent elastic moduli required to define a transversely isotropic medium are given.

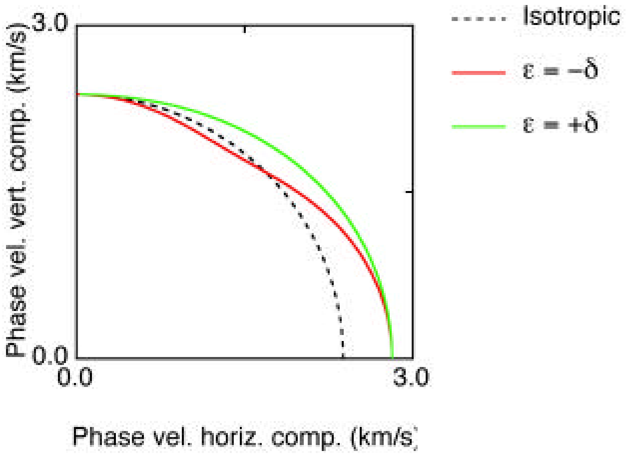

Fig. 2-4. Polar plot of qP mode phase velocity surface for an isotropic medium and for two Vertical Transversely Isotropic media, when $d = e = 0.2$ and when $d = -e = -0.2$ (after Thomsen, 1986). The vertical velocity of the qP mode is 2.35 km/s for the three surfaces. The two components are in km/s. Thomsen's parameter d has mainly an influence at near vertical propagation, whereas e determines velocity at horizontal incidence.

Table 2-2. Elastic moduli used to compute slowness surfaces of Figure 2-4, presented in Voigt notation (2-3). Only the five independent elastic coefficients required to define a transversely isotropic medium are shown. C_{44} and C_{66} are the same here because we only assume an anisotropic behavior for the qP mode.

Model\Coeffs	C_{11} (MPa)	C_{13} (MPa)	C_{33} (MPa)	C_{44} (MPa)	C_{66} (MPa)
Isotropic	14.91	4.33	14.91	5.29	5.29
$d = e = 0.2$	20.87	6.95	14.91	5.29	5.29
$d = -e = -0.2$	20.87	0.64	14.91	5.29	5.29

This review of the theoretical principles on anisotropy will allow us to build physically valid anisotropic models of the earth. In the following chapter, the ray-tracing algorithm is thoroughly described and the way it has been coded using a C++ object oriented programming approach is presented. Then the analytical method to build realistic anisotropic models is explained.

CHAPTER III

RAY TRACING BY WAVEFRONT CONSTRUCTION

Although the computations of ray path and travel times is the only aspect explicitly considered here, ray methods do compute all the information required for further applications (such as synthetic seismograms), i.e. ray path, travel time, amplitude and displacement vector (Babich, 1961; Cervený, 1972; Cervený, 2001). However, the method described in the previous section only provides this information along the ray and not in its vicinity. Thus, in the conventional ray-tracing approach (e.g. ray shooting or ray bending), we attempt to find the ray exactly connecting a source to a receiver. This process is iterative and requires a large amount of calculation, especially when a great number of source-receiver pairs is considered. In contrast, methods based on the paraxial approximation (Gibson, 1991) allow the extrapolation of the information carried by the ray to its near surroundings. A number of rays can therefore be propagated from the source throughout a bounded model regardless of receiver positions. Wavefront construction methods even go further by efficiently optimizing the density of rays (Lambaré at al., 1996; Vinje et al., 1993; Gibson, 2000). If the density of rays is reasonably high, travel times and amplitudes can be accurately extrapolated everywhere. This approach greatly increases the computational speed. However, among all the various wavefront construction methods proposed in the literature, Gibson’s (2000) is the only one explicitly considering general anisotropy. The new algorithm was developed using the C++ object oriented programming approach because it provides a great flexibility in the design of new components. This makes complex programs easy to debug and to maintain. However, before explaining this approach in great details and how it is used for developing the new software, one must understand the main steps of the wavefront construction, which will be our tool for the subsequent analysis of the VSP dataset.

The wavefront construction method

Figure 3-1 presents the basic principle of the wavefront construction algorithm, for a two-dimensional medium (Gibson, 2000). On the left side (Figure 3-1A) a fan of rays regularly spaced as far as the take-off angle is concerned is represented. The source is at the center and the gray ellipse is the wavefront at a propagation time of 1s. The medium is transversely isotropic and the corresponding elastic tensor is given in Table 3-1. If the location where we want to compute the information (i.e., the receiver location) falls between 2 rays, which is likely to occur, we want the density of rays to be high enough to extrapolate accurately. However, as one can see on Figure 3-1A, the ray density is reasonable at the wavefront, but way too high near the source. A more efficient approach would be to insert new rays at some distance from the source, as rays diverge and the space between them increases (Figure 3-1B). Once ray paths and wavefronts are computed, as shown in Figure 3-1B, the relevant information can be accurately interpolated anywhere in the zone of interest.

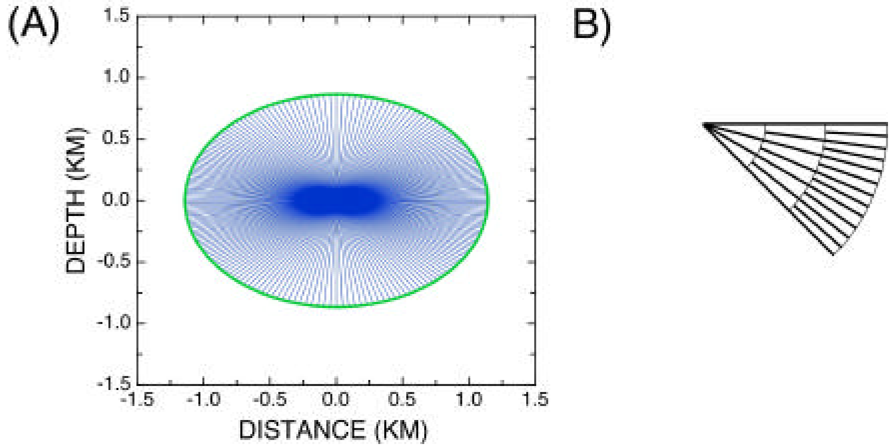

FIG. 3-1. (A) Fan of rays traced in a vertical plane using a constant increment of take-off angle. A wavefront at time one second is shown by the ellipse connecting ray end points. (B) Schematic illustration of a set of wavefronts (fine lines) and rays (heavy lines) that would be produced by a more efficient algorithm than the result shown in (A) (from Gibson, 2000).

Table 3-1: Elastic moduli C_{IJ} in GPa used for test calculations shown in Figure 3-1. Coefficients are in Gpa and use Voigt notation.

$$\begin{pmatrix} 3.52 & 2.68 & 2.03 & 0 & 0 & 0 \\ 2.68 & 3.52 & 2.03 & 0 & 0 & 0 \\ 2.03 & 2.03 & 2.02 & 0 & 0 & 0 \\ 0 & 0 & 0 & 0.31 & 0 & 0 \\ 0 & 0 & 0 & 0 & 0.31 & 0 \\ 0 & 0 & 0 & 0 & 0 & 0.42 \end{pmatrix}$$

The computation of rays and wavefronts can be decomposed in three major steps (after Gibson, 2000):

1/ *Initial fan of rays*

An initial sparse fan of rays is traced from the source as shown on Figure 3-2, for a three-dimensional medium. Rays are traced until they terminate (for example, when they reach an internal boundary or when they go outside the model bounding box) by numerical integration of the ray system (2-11) using a conventional Runge-Kutta method.

2/ *Wavefront mesh construction*

Wavefronts are simply constructed by linking neighboring rays at the corresponding time points (Figure 3-3). A time step is given by the user to regularly construct the wavefronts. As a result, the wavefronts are made of quadrilateral surface elements (or cells) in the three-dimensional space (only one cell is represented in Figure 3-2).

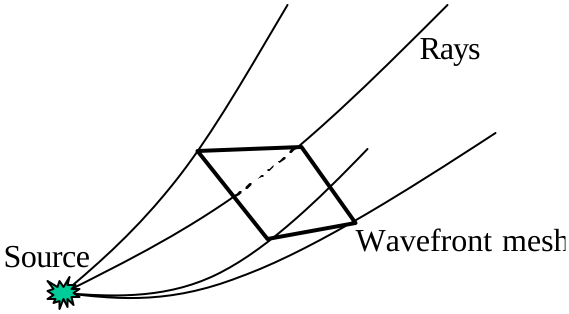

FIG. 3-2. Schematic illustration of an initial fan of rays (four in this case) traced from the source and a wavefront mesh, defined with quadrilateral surface elements in a three-dimensional space (after Gibson, 2000).

3/ *Wavefront interpolation*

The paraxial approximation expands the travel time of a point on a central ray with coordinates x'_i to a nearby location x_i, using a Taylor series (Gajewski and Pšencik, 1987; Gibson, 1991):

$$t(\vec{x}) = t(\vec{x}') + (x_j - x'_j) p_j(\vec{x}') + \frac{1}{2}(x_i - x'_i)(x_j - x'_j)\frac{\partial^2 t}{\partial x_i \partial x_j} \qquad (3\text{-}1)$$

Derivatives of travel time with respect to distance used in the first term of the development are equal to the components of the phase slowness vector, as shown in the above equation. Those components, as well as Cartesian coordinates of the travel path are known all along the ray. The second derivatives of travel time appearing in the second term of the development cannot be obtained directly and a finite difference technique is used. This computation involves quantities that have not been defined yet: the ray coordinates. The three ray coordinates in the three-dimensional space are two take-off angles f and y and the travel time t. Angle f is the declination and y is the azimuth (like in spherical coordinates). The initial fan of rays is produced by tracing rays at equal increment in declination and azimuth. Figure 3-3 presents a schematic view of one wavefront element built by the linking of four adjacent rays. Coordinates of the four ray points giving the corners of the quadrilateral surface element are expressed with ray coordinates. If the quadrilateral surface element is small enough (i.e. if the density of rays is reasonably high), derivatives of the ray points Cartesian coordinates and the slowness vector components with respect to take-off angles can be computed using a conventional finite difference approach. For instance, derivatives of the slowness vector components with respect to declination and azimuth are given by:

$$\frac{\partial p_i}{\partial f} \approx \frac{p_i^{(B)} - p_i^{(A)}}{\Delta f},$$

and (3-2)

$$\frac{\partial p_i}{\partial y} \approx \frac{p_i^{(D)} - p_i^{(A)}}{\Delta y},$$

where A, B and D are the ray points shown in Figure 3-3.
Derivatives of these quantities with respect to travel time are already known (right hand sides of the ray-tracing system 2-11).

Once derivatives of $\vec{p}$ and $\vec{x}$ with respect to ray coordinates are known, the second derivatives of travel time appearing in the second term of the Taylor series expansion (equation 3-1) can be calculated using the chain rule (Gajewski and Pšencik, 1987, Gibson, 1991):

$$\frac{\partial^2 t}{\partial x_i \partial x_j} = \frac{\partial p_i}{\partial x_j} = \left(\frac{\partial p_i}{\partial g_l}\right)\left(\frac{\partial x_j}{\partial g_l}\right)^{-1}, \qquad (3\text{-}3)$$

where g_l (l = 1, 2 and 3) are the ray coordinates f, y and t previously defined.

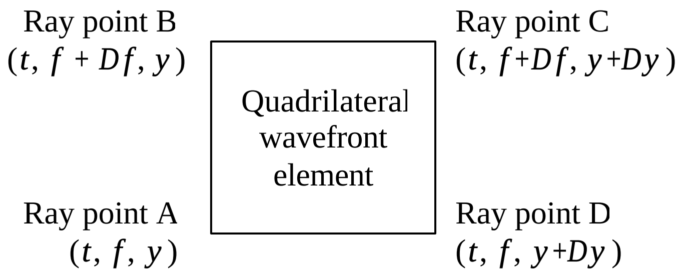

FIG. 3-3. Schematic representation of a quadrilateral wavefront surface element. The illustration is in two dimensions, but in three-dimensional media, wavefront elements are not necessarily contained in a plane. Initial rays are traced at equal increment in declination and azimuth (Df and Dy, respectively). For this reason, their position is defined using ray coordinates f, y and t that are the declination, the azimuth and the travel time along the ray, respectively. Travel time t is obviously the same for the four points because they lye on the same wavefront.

The first wavefront is constructed at the first time step (Figure 3-2) and each quadrilateral surface element is tested to see if a new ray needs to be inserted. To do this, we simply extrapolate the travel time in point C (Figure 3-3) using the paraxial approximation on the information known in point A, B and D (equation 3-1, 3-2 and 3-3). We compare the extrapolated time to t (value known from the computation of the ray going through point C). If the difference is greater than a predefined threshold value, rays are interpolated on the previous wavefront where the accuracy condition is still fulfilled (Figure 3-4). The starting time of an extrapolated ray is also computed using the paraxial approximation (equation 3-1) and its initial direction is linearly interpolated from the directions of the two surrounding rays. Because the interpolation is based on travel time error, which in turn is directly related to the curvature of the wavefront between rays, the mesh will automatically be refined in area where the wavefront changes the most rapidly (Gibson, 2000). The new wavefront and the interpolated rays are represented in gray on Figure 3-4. As a result, five new rays are created and the second wavefront has four cells. Wavefront are constructed and interpolated periodically to maintain a reasonable density of rays throughout the model. Once the wavefield is totally computed, travel time and amplitude can be extrapolated accurately anywhere in the model.

The above method is being developed using the C++ object oriented programming approach and before describing in further detail its implementation, it is necessary to give a brief explanation of the programming language.

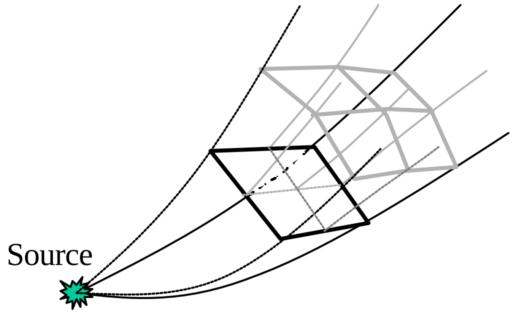

FIG. 3-4. Schematic illustration of the rays and wavefront mesh of Figure 3-2. The wavefront has been interpolated and as a result, the wavefront at the next time step has four cells. The new wavefront constructed and the interpolated rays are represented in gray.

The object oriented programming approach

In classic programming, programmers design sets of functions to process data or evaluate equations. This approach is called *procedural programming* because it emphasizes procedures rather than data. In contrast, *object-oriented programming* is an approach that "emphasizes the data rather than the procedure" (Stevens and Walnum, 2000). In this approach, the programmer creates his own data type; and functions and procedures to handle it are intrinsically attached to it. This process is called *encapsulation*. The abstract definition of encapsulated data structures and related functions is called a *class*. A class has two types of members. The private members are the affiliated variables and functions that can only be used and changed by internal procedures. Public members are variables and functions that can also be accessed from external subroutines. Consequently, the user has only access to the private members through the public members and access functions must be designed. Functions allowing to read and modify the private data members are called *getter* and *setter* functions, respectively. This system allows the programmer to code procedures that controls the access to the data. It also prevents the assignment of bad values to private variables (e.g. if a variable with the same name is used in another part of a program). This way, local variables used in different scopes cannot interfere whatsoever. This makes programs easier to write and to debug. Another advantage of this system is that local members related to a general class of action but with specific implementation can have the same name so a reader can easily understand the code. The compiler knows which member is called by knowing which class it refers to. This property of object oriented programming is called *polymorphism*. In the following, we present an example of a class definition to handle complex numbers (after Stroustrup, 1997):

```
class Cplx
{
//Declaration of the private members
private:
     float Real;     //real part
     float Im;  //imaginary part

//Declaration of the functions necessary to handle the
//Cplx data type
public:
     //this function allows the user to initialize
     //or to modify the private members (setter function)
     void Set(float x, float y);
     //functions returning the real and imaginary
     //(getter functions)
     float Real();
     float Im();
     //function that returns the norm
     float Norm();
}    //end of the class definition.
```

The above code is the abstract definition of a class named `Cplx`. It does not give the explicit implementation of the related procedures yet. Abstract class definitions are usually contained in a separate file named *header file*. This file can be consulted as documentation. It provides all the information that the user needs to know to work with the data type. A simple user does not need to know how class procedures are programmed and can concentrate on higher level implementations by simply calling them in his (or her) own code. For this reason, the explicit code of these functions is usually contained in another file (the access to which may be restricted):

```
//the setter function allows the user to initiate or
//change the private data members
void Cplx::Set(float x, float y){
     Real = x;
     Im = y;
}
//the getter functions allow the user to read the
//private data members
float Cplx::Real(){
     return Real;
}
float Cplx::Im(){
     return Im;
}
float Cplx::Norm(){
     float norm = sqrt(Real*Real + Im*Im);
     return norm;
}
```

In the main subroutine, the user can then define a variable of the `Cplx` type called `z`, just like he (or she) would do with a predefined data type such as `int` or `float`. The user can obtain the norm of the complex number `z` simply by calling the function `z.Norm()`. The user needs to call the function `z.Set(a,b)` to set the real and imaginary part (which are private members) of object `z` to `a` and `b` respectively. This technique also allows the programmer to insert commands ensuring that the object is properly initialized. The flexibility of object oriented programming goes even beyond that and also allows the developer to redefine the basic operator such as `()`, `*`, `+`, `-`, `/`, etc… For example, the operator `+` can be redefine to add independently real and imaginary parts of complex objects. However, an abstract data type and its member functions, once coded, define a sort of “black box” that cannot be adapted to new uses except by modifying its definition, which requires to modify and recompile the code each time a new functionality is added (Stroustrup, 1997). The object oriented programming approach easily solves this problem by one of its intrinsic properties named *inheritance*. To illustrate *inheritance*, we suppose that we want to create a new abstract data type allowing the user to handle polar form of complex numbers. The new class can simply be derived from the previous one:

```
//------------- Header file -------------------------
//The new PolCplx class inherits from Cplx
class PolCplx : public Cplx
{
//Declaration of the private members specific to the
//derived class
private:
     float Rho;      // radius
     float Teta;     // angle
//Declaration of the function necessary to handle the
//PolCplx data type
public:
     //this function allows the user to initialize
     //or to modify the private members
     void Set(float r, float t);
}    //end of the class definition

//----------------- Procedures file ---------------------
//Follows the procedure for the above declared function
void PolCplx::Set(float r, float t){
     Real = r*cos(t);
     Im = r*sin(t);
     Rho = r;
     Teta = t;
}
```

The new data type called `PolCplx` inherits from data type `Cplx` and therefore has the same private and public members, and new ones. For instance, one can define an object named `zpol` of type `PolCplx` and call function `zpol.Norm()`. But the new data type brings some new capabilities without requiring change in the code related to the `Cplx` data type. The class `Cplx`, in this case, is the base class or the mother class of the `Cplx` class hierarchy. Function `zpol.Set()` illustrate the principle of polymorphism. The `zpol.Set()` command calls the setter function defined in the `PolCplx` class and not the one defined in the `Cplx` class.

The C++ object oriented programming approach also allows the programmer to declare functions in the mother class, only implementing procedures for these functions in the derived class by using the command `virtual`. The mother class can then contain generic procedures common to all the derived classes, which require calls to functions that depend on the specificity of the derived class and are therefore implemented in a lower level of the class hierarchy. For example, in this project, as it will be explained with more details later in this chapter, a base class named `Ray` has been defined that computes and stores an individual ray. To compute a ray at a given location (x, y ,z), the elastic moduli at this point are obviously needed. However, the coding of the function returning this information depends on the model we consider and we do not want to change the code related to the nucleus of the algorithm (such as the `ray` class that integrates ray-tracing system 2-11) each time a new model is built. Hence, the following lines are inserted in the declaration of the abstract class `Ray`:

```
// Declaration of the function returning model parameter
virtual CurrentParams(float x, float y, float z);
```

Calls to this function can be made in all the procedures of the base class `Ray`. When a new model is considered, a class inheriting from class `Ray` can be declared and the procedure for the function `CurrentParams` explicitly coded in the new class definition.

To summarize, an object-oriented program has four fundamental characteristics (Stroustrup, 1997; Schildt, 1998; Stevens and Walnum, 2000):

- *Abstraction* defines a new data type, like the above examples. An abstract base class can be defined that contains the general data or to manipulate the data.
- *Encapsulation* gathers all the different representations of a data type into the same entity. In other words, data and the procedures to manipulate it are bound together in an object. The procedures (functions) and the data contained in this object may be private or public. If data or procedures are declared as private, they cannot be accessed from a procedure that is external to the object. This allows the programmer to avoid outside interference or misuse. The public members can be used as an interface to control the private members.
- *Inheritance* is the process by which a new object is derived from an existing one. The new class will have the same characteristics as the mother class, but will add some qualities that are specific to it. Derived object classes and their abstract base class form a class hierarchy. For instance, if two object classes have some data or procedures in common, this common part can be coded into a base class and the two classes can be derived from it. Each of the two derived classes specifies its own characteristics into its definition.
- *Polymorphism* allows a general class of actions to have the same name, even though the local procedures change according to the characteristics of the derived class. Virtual functions can be declared in the abstract declaration of the base class and be defined later in the derived (inherited) classes according to their specificities.

Another important aspect of C++ object-oriented programming is the *template*. It allows the programmer to describe a generic data type or a generic function to manipulate any types of object. A typical class template is a vector, which is part of the C++ Standard Template Library (standard and generic classes built in the C++ language and automatically recognized by the compiler). A vector is a generic list of elements of any type. Procedures that are independent from the type of elements considered are encapsulated in the vector template class definition.

```
Template<class Element> class vector{
//private members of the class template
private:
     //Pointer to the first element of the vector
```

```
        Element* s
        //Integer containing the size of the vector
        int size
//The public members of the vector template class are
//the generic procedures that do not depend on the type
//of element we consider.
public:
        //Allows to define the size of a vector
        void Resize(int s);
        //Allows to add a new element at the end of the list
        void Push_back(Element e);
        // …
} //End of the class template definition
```

In the above code, the type of the class `Element` has not been given yet. Now, for instance, the programmer can use the functions encapsulated into the `vector` class template by declaring a vector of complex elements previously defined:

```
//Declares a vector of complex elements
vector<Cplx> myVector;
//Declares a complex number
Cplx z;
//Initializes the complex number z to 1+2i
z.Set(1.0, 2.0);
//Adds the complex number z to the vector myVector
myVector.Push_back(z);
```

Class templates are typically used ‘to build general-purpose container classes, in which the maintenance of the container is generic, but the item in the container is specific’ (Stevens and Walnum, 2000). C++ templates have been used to design the heart of the algorithm, which is the template class *RayField*. This class, as it is explained with further details in the next sub-chapter, can build wavefronts and ray fields from any type ray (isotropic, anisotropic, etc…). Another aspect of the project that motivates the use of template is parallel computation. A special implementation of Standard Template Library (STL) called Standard Template Adaptive Parallel Library (STAPL) (An et al., 2000), can take advantage of objects stored in STL classes to facilitate parallelization. This aspect is currently under development in the Texas A&M Computer Science Department. In a near future, the algorithm will be able to adapt itself to hardware configuration for maximum computational speed. For instance, the software will automatically detect the possibilities of the computational environment at run time on massively parallel supercomputers and partition data calculations accordingly.

After this brief introduction to C++ object oriented programming, we can describe in details how the algorithm by wavefront construction method has been implemented.

The class hierarchies of the algorithm

There are three main class hierarchies in the ray-tracing algorithm by wavefront construction method:

- The *EarthModel* hierarchy that contains all the information and all the functions relatives to the elastic properties of the medium.
- The *Ray* hierarchy that contains all the functions to trace an individual ray and all the variables to store it.
- The *RayField* class template (that is not a hierarchy strictly speaking) is actually the nucleus of the algorithm, since it codes the functions to build and store the ray field. That includes the fan of rays and the wavefronts. The *RayField* class template stores data related to a fan of rays propagating in any type of earth model and defines the generic procedures to manipulate it.

In the following, the three main class hierarchies and the general structure of the algorithm is described in further details (a different color is used for each class hierarchy and a class description indented from the previous one means inheritance):

RAY class (Figure 3-5)

Virtual base class of the *Ray* hierarchy that contains the basic organization of a seismic ray. The private members include vectors of data storing the Cartesian coordinates of the ray path and the slowness vector, and the travel time at each point along the ray. This class also has members, which are not strictly necessary for the computation of an individual ray. They are necessary to build a ray mesh, such as variables storing indices of neighboring rays in the mesh.

ANIRKRAY class

Virtual class that defines procedures for functions *Trace* and *RayDerivs*. The latter computes the right hand side of ray-tracing system (2-11). The function *Trace* integrates them using a Runge-Kutta algorithm.

HOMOGANIRKRAY class

End member of the class hierarchy for a ray propagating in a homogeneous model. It mainly stores a pointer to the homogeneous earth model and calls its functions.

Ray classes handling rays propagating in heterogeneous anisotropic models

End members of the class hierarchy for a ray propagating in the heterogeneous models developed in this project. These classes mainly store a pointer to the heterogeneous earth model object and call its functions.

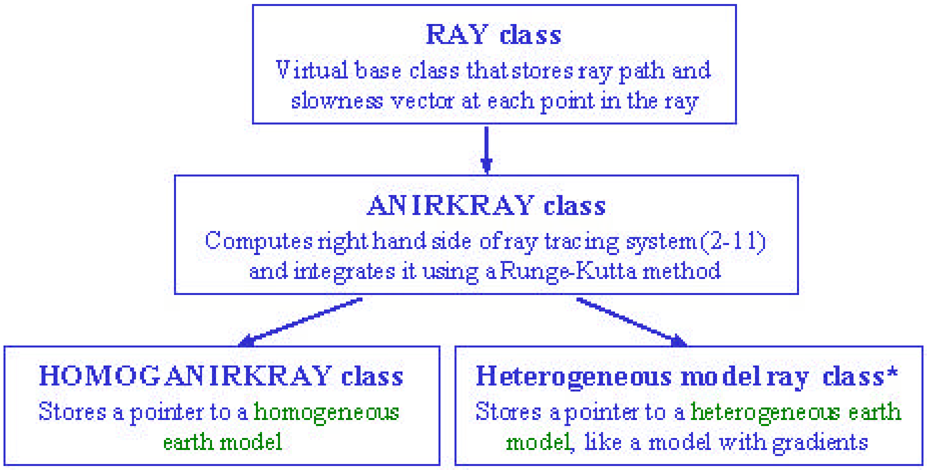

FIG. 3-5.The Ray class hierarchy. Arrows indicate inheritance between classes and the asterisk indicates the parts that were specifically built during this project.

EARTHMODEL class (Figure 3-6)

This is a base class of the *EarthModel* hierarchy. Currently, this class has no specific contents.

ANIEARTHMODEL class

Virtual class that stores elastic coefficients and density of the earth model. The elastic parameters are given by a 6 by 6 matrix of elastic coefficients (Voigt Notation given by equation 2-3).

HOMOGANIEARTHMODEL class

End member of the class hierarchy for a homogeneous model. It defines basically the function *CurrentParams*, returning the elastic moduli and its derivatives at the current location and the function *TestRayLocation* that check if a ray actually reached a termination point, such as a discontinuity or a model boundary.

Earth model classes handling heterogeneous anisotropic models

End members of the class hierarchy for heterogeneous models. They define the function *CurrentParams* returning the elastic moduli and its derivatives at the current location and the function *TestRayLocation* that checks if a ray actually reached a termination. The design of these classes is the major component of the first part of the project and is described in further detail in the following sub-chapter.

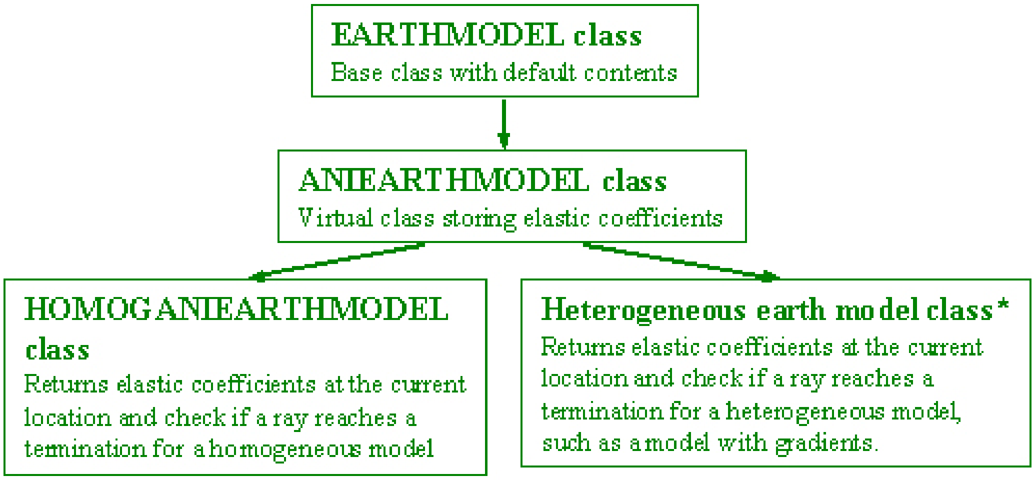

FIG. 3-6.The EarthModel class hierarchy. Arrows indicate inheritance between classes and the asterisk indicates the parts that were specifically built during this project.

RAYFIELD class

This class is actually a class template that builds the ray field for any type of ray (i.e., for rays propagating in any type of medium).

It stores the following information:

1/ A vector of ray objects containing all the rays propagating in the subsurface. Each ray object contains a variable pointing to the earth model object.

2/ A vector object containing all the wavefronts in the model. Each wavefront is made of a vector of quadrilateral elements.

It performs the following tasks:

1/ Trace all the initial rays by calling the *Trace* function of the ray class hierarchy. Rays are integrated using the Runge-Kutta method and the function *CurrentParams* of the earth model class is called to obtain the local information on the earth model and the function *TestRayLocation* is called to test if the ray must be terminated.

2/ Build the wavefront by linking the neighboring rays at the current time, into quadrilateral surface elements.

3/ Test each quadrilateral element to see if an interpolation is needed (Figure 3-4).

4/ If yes, extrapolate starting point for a new ray using the paraxial approximation (Equation 3-1) and interpolate a slowness vector from the two adjacent rays.

5/ Once this is done, trace the new ray from the interpolated starting point by calling the *Trace* function, which calls the functions *CurrentParams* and *RayTestLocation*.

6/ Loop over the wavefront time, until the maximum time is reach (return to step 2).

The new earth model classes were also implemented using a C++ object oriented programming approach and inserted in the algorithm. Specifically two main classes were developed: a single gradient and a multi-gradient anisotropic earth model classes.

Single gradient anisotropic earth model

One of the primary goals of this thesis was to build a realistic anisotropic earth model so that the ray-tracing method described at the beginning of this chapter could be used to simulate travel times of a field dataset. As previously said, the high-frequency approximation implies that the medium is smoothly inhomogeneous. In other words, if elastic coefficients vary with spatial coordinates, they must not vary greatly within a wavelength and they must be continuous as well as their derivatives. The simplest smoothly heterogeneous anisotropic earth model is an anisotropic material where the velocity varies linearly with depth. This is generally the first realistic assumption on the heterogeneity of the crust and the earth mantle (Popov and Camerlynck, 1996; Miller at al., 1997; Julia et al., 1998; Mitchell, 1998; Bostock, 1999; Hansen et al., 1999; Muller et al., 2000; Tittgemeyer et al., 2000; Darbyshire et al., 2000; Mereu, 2000; Wang et al., 2000; Dean et al., 2000; among others). As previously said, the most frequently encountered type of anisotropy in nature is Vertical Transverse Isotropy (hexagonal symmetry system Figure 2-1 and Table 2-1). Hence, most of the time, we will consider this type of anisotropy, even though all the equations and more generally the model classes that have been built during this project remain valid for all type of anisotropy (including isotropy). Because we want the velocity to vary linearly with spatial coordinates, we have the following expression for the vertical velocity of the quasi-P wave:

$$v_{pv}(x,y,z)=v_{pv}(0,0,0)+ax+by+gz\,, \tag{3-4}$$

where constants a, b and g are the derivatives of the vertical quasi-P wave velocity with respect to x, y and z respectively. Using this form, we derive the expression of the corresponding density normalized elastic coefficient a_{33} (equation 2-13 and 2-7) as a function of the spatial coordinates:

$$a_{33}(x,y,z)=\left[\sqrt{a_{33}(0,0,0)}+ax+by+gz\right]^2. \tag{3-5}$$

A Vertical Transversely Isotropic (VTI) medium has 5 independent elastic coefficients in the general case (hexagonal symmetry, Table 2-1). Therefore, we could introduce 5 x 3 = 15 independent gradients. However, we want the ratio of the horizontal velocity and the vertical velocity for the three mode of propagation to remain constant throughout the profile, as well as the ratio between the quasi-S and the quasi-P velocities (the quasi-S velocity must not exceed the quasi-P velocity). This way, we ensure that the model remains physically valid everywhere. In terms of elastic moduli, the above condition can be expressed the following way:

$$a_{ij}(x,y,z)/a_{33}(x,y,z)=const\,, \qquad \forall x,y,z\,. \tag{3-6}$$

The above condition can be enforced by simply introducing some weights w_{ij} in Equation (3-5), as follows:

$$a_{ij}(x,y,z)=\left[\sqrt{a_{ij}(0,0,0)}+w_{ij}(ax+by+gz)\right]^2, \tag{3-7}$$

with

$$w_{ij} = a_{ij}(0,0,0)/a_{33}(0,0,0). \qquad (3\text{-}8)$$

The first derivatives of elastic coefficients a_{ij} (required by system 2-11) are simply given by:

$$a_{ij,x}(x,y,z) = 2aw_{ij}\left[\sqrt{a_{ij}(0,0,0)} + w_{ij}(ax + by + gz)\right],$$

$$a_{ij,y}(x,y,z) = 2bw_{ij}\left[\sqrt{a_{ij}(0,0,0)} + w_{ij}(ax + by + gz)\right], \qquad (3\text{-}9)$$

and

$$a_{ij,z}(x,y,z) = 2gw_{ij}\left[\sqrt{a_{ij}(0,0,0)} + w_{ij}(ax + by + gz)\right].$$

As a result, the user simply has to specify the values of the elastic coefficients $a_{ij}(0,0,0)$ and the three spatial gradients for the vertical quasi-P velocity, i.e. a, b and g. A test is performed inside the constructor (the C++ function that initializes the object variable), to ensure that the elastic tensor is symmetric. From Equations (3-7) and (3-8), the following implication can be easily shown:

$$a_{11}(0,0,0) = a_{12}(0,0,0) + 2a_{66}(0,0,0) \;\Rightarrow\; a_{11}(x,y,z) = a_{12}(x,y,z) + 2a_{66}(x,y,z). \qquad (3\text{-}10)$$

More generally, any linear relationship between elastic coefficients remains true everywhere in the model. Hence, Equations (3-7) and (3-8) also ensure that the medium will keep the same type of anisotropy along the profile. For instance, if the user initializes the model with a set of elastic coefficients of a VTI medium, these elastic coefficients will vary with spatial coordinates in such a way that the velocity varies linearly, and that the medium remains VTI anywhere. This solution allows us to avoid cumbersome code development to handle different types of anisotropy. Equations presented in this section are valid for any type of anisotropy. Only the starting values of elastic coefficients set the type of anisotropy anywhere in the model. Furthermore, we want to perform as few computations as possible inside the function *CurrentParams* because it is called a great number of times. This solution involves little algebra and requires the storage of very few parameters (a 6-by-6 matrix and three gradients) unlike a model defined by a grid.

Another consequence of this approach is that in the particular case of a transversely isotropic medium, the Thomsen's parameters (equations 2-12 and 2-18) remain constant throughout the model. An overloaded version of the constructor allows the user to initialize the object by using Thomsen's parameters instead of using an elastic tensor (obviously, it must only be used in the case of a transversely isotropic medium). Besides the constructor, *CurrentParams* and *TestRayLocation*, other functions have been implemented that are not strictly necessary for the ray tracing, such as functions returning phase velocity, group velocity, as well as one-dimensional and two-dimensional velocity profiles, and elastic moduli profiles. Figure 3-7 presents the five independent elastic moduli for a VTI model where velocities vary only with depth. The depth gradient for the quasi-P velocity is 0.71 km/s/km. The vertical quasi-P and quasi-S velocities at the origin are 1.719 km/s and 0.7 km/s respectively (for a Vertical Transverse Isotropic medium, vertical quasi-S1 and quasi-S2 velocities are the same) and Thomsen's parameters are $e = 0.1$, $d = 0.2$ and $g = 0.1$. As a result, the anisotropy (i.e., the ratio between horizontal and vertical velocity) for quasi-P mode is 8.7%. Figure 3-8 presents the corresponding horizontal and vertical velocities for the three modes. Figure 3-9 presents a wavefront traveling in the medium described above after 0.8s of propagation, for a source depth of 10 kilometers. The quadrilateral elements of the wavefront link the rays together. The wavefront is not spherical, because of the anisotropy and inhomogeneity of the earth model. It is slightly stretched horizontally and dilated downward, where the velocity increases. The computation time for this case was 16s on a SUN Sparc III.

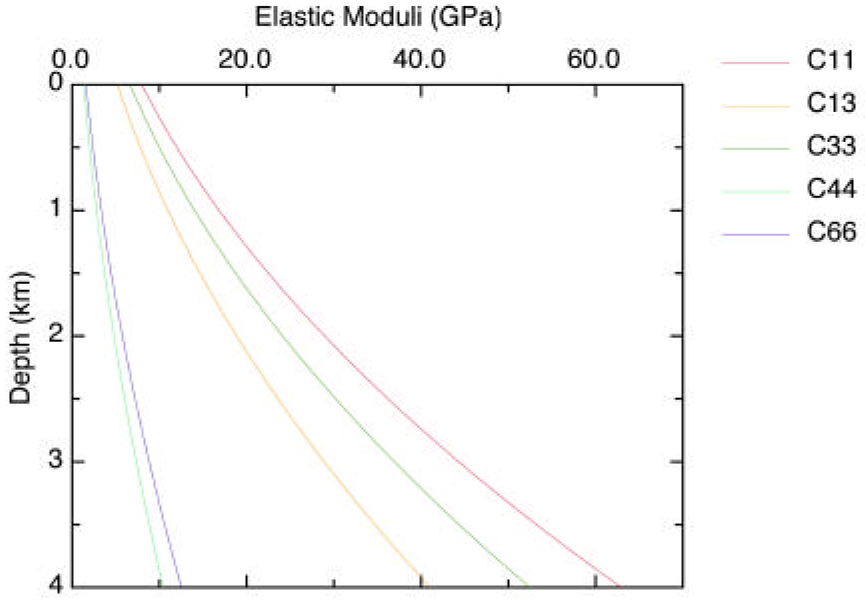

FIG. 3-7. The five independent elastic moduli for a synthetic Vertical Transversely Isotropic medium where the velocity varies linearly with depth. Vpv(0,0,0) = 1.719 km/s, Vsv(0,0,0) = 0.7 km/s, $e = 0.1$, $d = 0.2$ and $g = 0.1$. The depth gradient for the quasi-P velocity is 0.71 km/s/km. The corresponding Initial values for the five elastic moduli are the following: $C_{11} = 7.98$ GPa, $C_{13} = 5.20$ GPa, $C_{33} = 6.65$ GPa, $C_{44} = 1.32$ GPa and $C_{66} = 1.59$ GPa (with $r = 2.7$ g/cm^3).

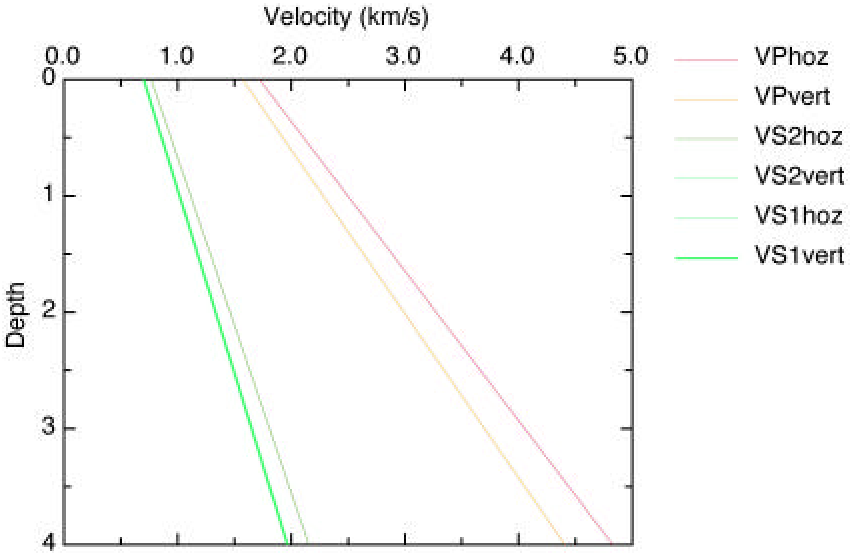

FIG. 3-8. Vertical and horizontal velocities in function of depth, for the three modes of propagation in the same model described in Figure 3-7.

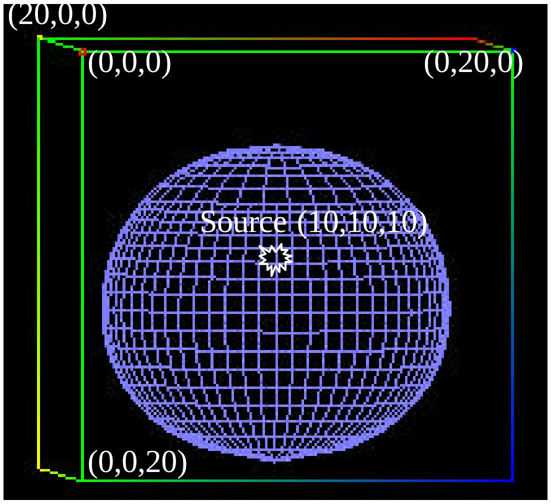

FIG. 3-9. Wavefront propagating in the inhomogeneous anisotropic medium described above, with a source depth of ten kilometers. The propagation time is 0.8s. Labeling is in kilometers.

Multi-layered anisotropic earth model

Another class was also designed to provide models of a multi-layered anisotropic earth. Each layer is described by the same equations that have been used to build the single gradient earth model class. Implementation of a class containing discontinuities such as interfaces is feasible but appropriate modifications of the heart of the ray-tracing algorithm would be needed. Indeed, across discontinuities the elastic coefficients are discontinuous and therefore their derivatives are not defined. The direct consequence is that the right hand side of the ray tracing system (2-11) is not defined and the ray trajectory cannot be computed using this technique. Instead, a system of equations involving reflection and transmission coefficients must be solved. These equations are established by the continuity of stress and movement across the interface. Although the concept is well understood (Aki and Richard, 1980; Cervený, 2001), the coding is complicated and, at this stage the algorithm can only sustain smoothly inhomogeneous media. Furthermore, we focus on Vertical Seismic Profiles which means that we mainly deal with direct waves and not with reflected waves. Thus, this assumption is not very restrictive in our case. Consequently, the elastic moduli and their derivatives must be continuous throughout the model. Hence, smoothing functions must be introduced at each interface (Figure 3-10). The thickness of the smoothed transition zone is determined by the wavelength of the seismic wave. Specifically, this thickness must be greater than the longest wavelength contained by the seismic signal. For instance, if the velocity is 2km/s and the lowest frequency is 10Hz, the transition zone must be at least 200m thick.

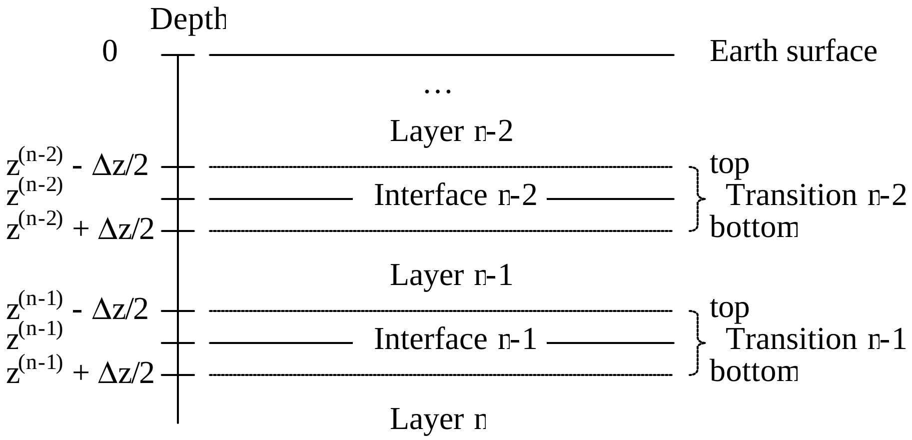

FIG. 3-10. The multi-layered model made by a succession of layers where the velocity varies linearly with depth. Elastic moduli must vary smoothly with spatial coordinates (high frequency approximation, equation 2-5) and smoothed transition zone must be introduced at the interfaces.

Elastic coefficients in layer *n* are given by the continuity of the elastic coefficients at interface *n-1* and the gradient in layer *n*. Elastic coefficients of layer n-1, layer n and smoothed transition zone at interface n-1 (Figure 3-10) can then be expressed as:

$$A_{ij}^{(n-1)}(x,y,z) = \left\{\sqrt{a_{ij}^{(n-1)}} + w_{ij}\left[ax + by + g^{(n-1)}\left(z - z^{(n-2)}\right)\right]\right\}^2, \tag{3-11a}$$

$$\forall z \in \left[z^{(n-2)} + \Delta z/2\,, z^{(n-1)} - \Delta z/2\right[\,;$$

$$A_{ij}^{smooth}(x,y,z) = s_{ij}^{(1)} z^5 + s_{ij}^{(2)} z^4 + s_{ij}^{(3)} z^3 + s_{ij}^{(4)} z^2 + s_{ij}^{(5)} z + s_{ij}^{(6)}, \tag{3-11b}$$

$$\forall z \in \left[z^{(n-1)} - \Delta z/2, z^{(n-1)} + \Delta z/2\right[\,;$$

$$A_{ij}^{(n)}(x,y,z) = \left\{\sqrt{a_{ij}^{(n)}} + w_{ij}\left[ax + by + g^{(n)}\left(z - z^{(n-1)}\right)\right]\right\}^2, \tag{3-11c}$$

$$\forall z \in \left[z^{(n-1)} + \Delta z/2\,, z^{(n)} - \Delta z/2\right[\,;$$

where $s_{ij}^{(1->6)}$ are the six coefficients of the smoothing functions (independent of *z*);

$z^{(n-1)}$ is the depth of interface *n-1*;

Δz is the thickness of the smoothed transition zone;

$g^{(n)}$ is the derivative of the vertical quasi-P velocity with respect to z in layer *n*;

and elastic coefficients $a_{ij}^{(n)}$ are derived recursively such that

$$A_{ij}^{(n+1)}\left(x, y, z^{(n)}\right) = A_{ij}^{(n)}\left(x, y, z^{(n)}\right), \qquad \text{for } n = 1, \ldots, n_{\max} \tag{3-12}$$

Hence,

$$\sqrt{a_{ij}^{(n+1)}} = \sqrt{a_{ij}^{(n)}} + w_{ij} g^{(n)}\left(z^{(n)} - z^{(n-1)}\right), \quad \text{for } n = 1, \ldots, n_{\max} \tag{3-13}$$

At the bottom and the top of the smoothing transition between layer *n* and *n-1*, the continuity of each elastic coefficient, its first derivative and its second derivative with respect to *z* provides a system of six equations with six unknowns giving coefficients of the smoothing functions $s_{ij}^{(1->6)}$ (equation 3-11b):

$$A_{ij}^{smooth}\Big|_{top} = A_{ij}^{(n-1)}\Big|_{top} = \left\{\sqrt{a_{ij}^{(n-1)}} + w_{ij}\left[ax + by + g^{(n-1)}\left(z^{(n-1)} - z^{(n-2)} - \Delta z/2\right)\right]\right\}^2,$$

$$A_{ij}^{smooth}\Big|_{bottom} = A_{ij}^{(n)}\Big|_{bottom} = \left\{\sqrt{a_{ij}^{(n)}} + w_{ij}\left[ax + by + g^{(n)}\,\Delta z/2\right]\right\}^2,$$

$$\partial A_{ij}^{smooth}/\partial z\Big|_{top} = \partial A_{ij}^{(n-1)}/\partial z\Big|_{top} =$$

$$2 w_{ij} g^{(n-1)}\left\{\sqrt{a_{ij}^{(n-1)}} + w_{ij}\left[ax + by + g^{(n-1)}\left(z^{(n-1)} - z^{(n-2)} - \Delta z/2\right)\right]\right\},$$

$$\partial A_{ij}^{smooth}/\partial z\Big|_{bottom} = \partial A_{ij}^{(n)}/\partial z\Big|_{bottom} = 2 w_{ij} g^{(n)}\left\{\sqrt{a_{ij}^{(n)}} + w_{ij}\left[ax + by + g^{(n)}\,\Delta z/2\right]\right\}, \tag{3-14}$$

$$\partial^2 A_{ij}^{smooth} \big/ \partial z^2 \Big|_{top} = \partial^2 A_{ij}^{(n-1)} \big/ \partial z^2 \Big|_{top} = 2\left(w_{ij} g^{(n-1)}\right)^2,$$

and

$$\partial^2 A_{ij}^{smooth} \big/ \partial z^2 \Big|_{bottom} = \partial^2 A_{ij}^{(n)} \big/ \partial z^2 \Big|_{bottom} = 2\left(w_{ij} g^{(n)}\right)^2,$$

where top and bottom pertain to the transition zone, i.e. to $z = z_1 = z^{(n-1)} - \Delta z/2$ and $z = z_2 = z^{(n-1)} + \Delta z/2$, respectively. Because we have six equations, we need six unknowns and therefore, functions used to smooth interfaces are polynomials of the 5th degree. We want the second derivatives to be continuous as well since it may be required by the computation of amplitude (Cervený et al., 1977). For each independent elastic modulus, the resulting system expressed with matrices is the following:

$$\begin{pmatrix} z_1^5 & z_1^4 & z_1^3 & z_1^2 & z_1 & 1 \\ z_2^5 & z_2^4 & z_2^3 & z_2^2 & z_2 & 1 \\ 5z_1^4 & 4z_1^3 & 3z_1^2 & 2z_1 & 1 & 0 \\ 5z_2^4 & 4z_2^3 & 3z_2^2 & 2z_2 & 1 & 0 \\ 20z_1^3 & 12z_1^2 & 6z_1 & 2 & 0 & 0 \\ 20z_2^3 & 12z_2^2 & 6z_2 & 2 & 0 & 0 \end{pmatrix} \begin{pmatrix} s_{ij}^{(1)} \\ s_{ij}^{(2)} \\ s_{ij}^{(3)} \\ s_{ij}^{(4)} \\ s_{ij}^{(5)} \\ s_{ij}^{(6)} \end{pmatrix} = \begin{pmatrix} A_{ij}^{(n-1)} \Big|_{top} \\ A_{ij}^{(n)} \Big|_{bottom} \\ \partial A_{ij}^{(n-1)} \big/ \partial z \Big|_{top} \\ \partial A_{ij}^{(n)} \big/ \partial z \Big|_{bottom} \\ \partial^2 A_{ij}^{(n-1)} \big/ \partial z^2 \Big|_{top} \\ \partial^2 A_{ij}^{(n)} \big/ \partial z^2 \Big|_{bottom} \end{pmatrix}. \qquad (3\text{-}15)$$

The six by six matrix on the left hand side of the system depends only on the depth of interfaces (and the thickness of the smoothing transition zone, which is assumed to be a constant) and is inverted in the constructor of the anisotropic earth model class. However, the multiplication by the vector on the right hand side of the system, which depends on x and y coordinates as well must be done inside the *CurrentParams* function each time moduli are computed. The other outputs of the function are the spatial derivatives of the elastic coefficients. Although they are straightforward inside a layer where the velocities vary linearly (equation 3-11a), their analytical expressions are tedious to derive inside the transition zone (equation 3-11b). Indeed, the six coefficients of smoothing functions at each interface depend on spatial coordinates. Expressions for those derivatives are given in appendix.

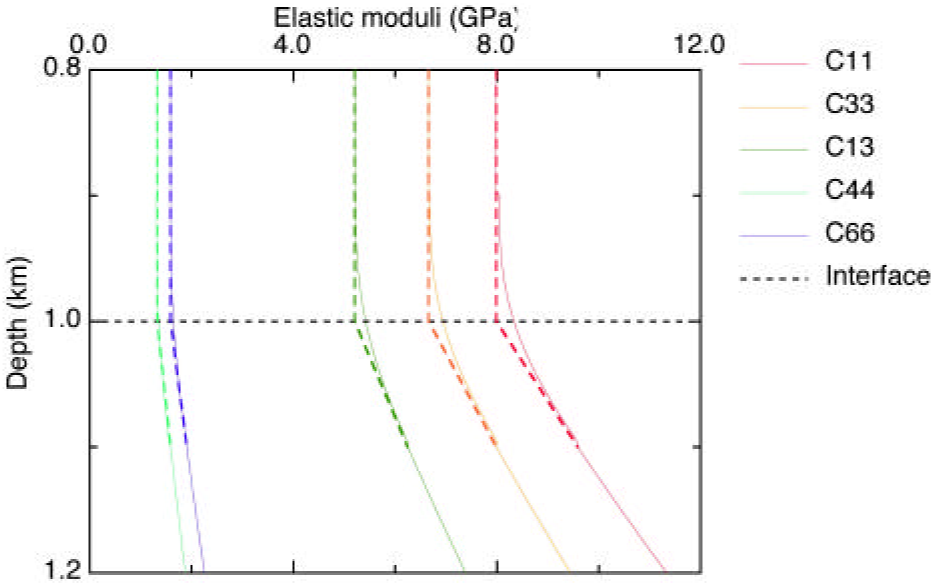

FIG. 3-11. The five independent elastic moduli in function of depth for the VTI medium with two gradients. The interface is at 1 km depth, the first layer is homogeneous while the second one has a strong velocity gradient. The elastic coefficients have been smoothed by a 5-degree polynomial at the interface so that their first and second derivatives with respect to depth are continuous. In this example, Thomsen's parameters are the following $e = 0.1$, $d = 0.2$ and $g = 0.1$. The gradient of the second layer is 1.5 km/s/km, the starting vertical velocities are 1.7 km/s and 0.7 km/s for the quasi-P and the quasi-S modes respectively. Initial values for the five elastic moduli are the following: C_{11} = 7.98 GPa, C_{13} = 5.20 GPa, C_{33} = 6.65 GPa, C_{44} = 1.32 GPa and C_{66} = 1.59 GPa.

Figure 3-11 shows elastic coefficients in a medium with two layers. The whole medium is Vertical Transversely Isotropic, but the first layer is homogeneous whereas the second has a strong positive gradient. One can see the smoothing transition with a thickness of 200 meters in this case. Colored dashed lines show the extension of curves when there is no smoothing transition. The black dashed line represents the depth of the interface at one kilometer. Values of each elastic coefficient are defined only by these linear trends. The smoothing functions do not influence the values of elastic moduli within each layer. Figure 3-12 shows derivatives with respect to z of the five independent elastic moduli presented in Figure 3-11. In Figure 3-13, one can see a wavefront propagating in the medium of Figure 3-11 and 3-12. The gradient of the second layer (1.5 km/s/km) has been exaggerated to emphasize the presence of the interface. The source depth is 500 meters, in the middle of the homogeneous layer on the top. The wavefront corresponds to a travel time of 1.5 seconds. One can clearly see the wave transmitted in the second layer and the refracted wave in the first layer. Like in Figure 3-9, the presence of anisotropy (8.7%) makes the wavefront in the second layer non-spherical. It expands more rapidly in the horizontal direction. This example also shows that even though the high frequency approximation is restrictive, the algorithm is robust enough to allow wavefield computation in realistically heterogeneous medium. This method allowing to build multi-gradient models in depth can also be used to build models with several gradients in x- or y- directions also (for example a syncline or anticline model). This can be simply done by considering vertical layer and therefore by changing the role of x- (or y-) component with z- component.

Chapter II made a review of the theory of anisotropic wave propagation and helped us to build physically valid synthetic earth models. The method described above allows us to analytically build anisotropic class model with little algebra. However, this knowledge is not enough to design realistic models simulating the earth subsurface and the next chapter provides an insight on real cases of anisotropy.

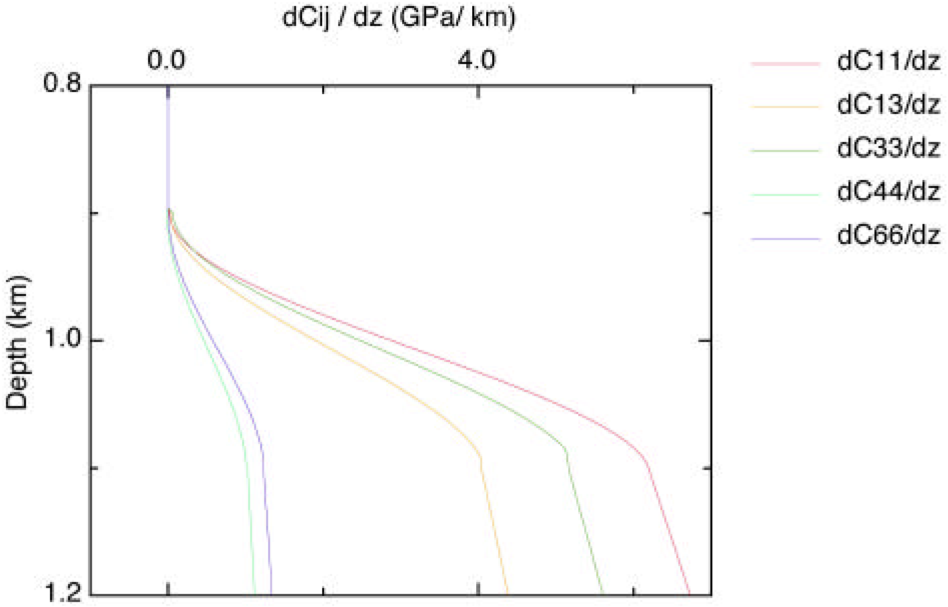

FIG. 3-12. Derivatives of the five independent elastic moduli presented in Figure 3-11 with respect to depth.

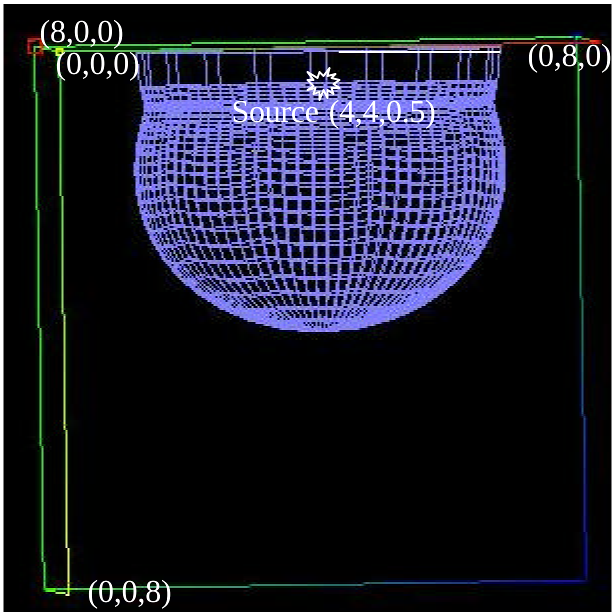

FIG. 3-13. Wavefront propagating in the two gradient anisotropic medium described above at time t = 1.5s. The source depth is 0.5 km. The presence of the interface is clearly visible on the picture. Because the second layer is faster than the first one, the wave propagating above the interface is refracted while the one propagating below is transmitted. Labeling is in kilometers.

CHAPTER IV

ANISOTROPY: EXAMPLES FROM THE GULF OF MEXICO

Extensive field measurements on anisotropy were recently made (Shuck, 1991; Kendall and Raymer, 1999; Raymer et al., 1999; Sriram et al. 1983; Thomsen 1986; Wetzel 1987; Winterstein, 1986; Hilterman et al., 1998; among others) and we summarize several examples to provide insight into real case studies of anisotropy in order to build realistic synthetic models. This knowledge also gives estimation on a range of anisotropy to expect in a field dataset. We mainly focused on some examples from the Gulf of Mexico.

Salt anisotropy in the Mahogany field

Even though salt has very high seismic velocities, it is very buoyant and deformable which allows it to flow easily. An important consequence of such flow is that the salt body crystals can align, therefore generating an effective seismic anisotropy (Raymer and Kendall, 1998). The most extensive study on salt anisotropy was performed in the Mahogany field. This field is located in the Gulf of Mexico (Figure 4-1).

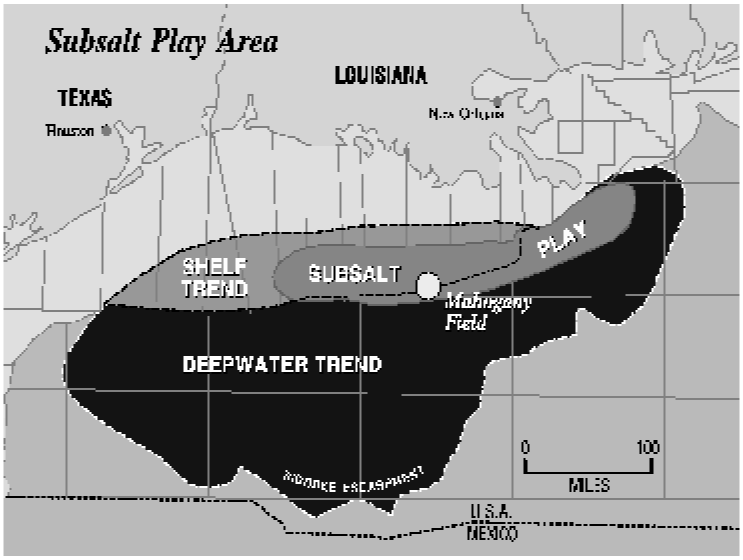

FIG. 4-1. Subsalt play area and Mahogany field location, Gulf of Mexico (from Camp, 1997).

This subsalt main geological feature has been interpreted to be a faulted anticline and the prospect, producing oil from three sand layers, is approximately 4300 meters deep (Kendall and Raymer, 1999). A seismic section showing the salt body is presented in Figure 4-2. The salt body is approximately 10 km long and 1 km thick.

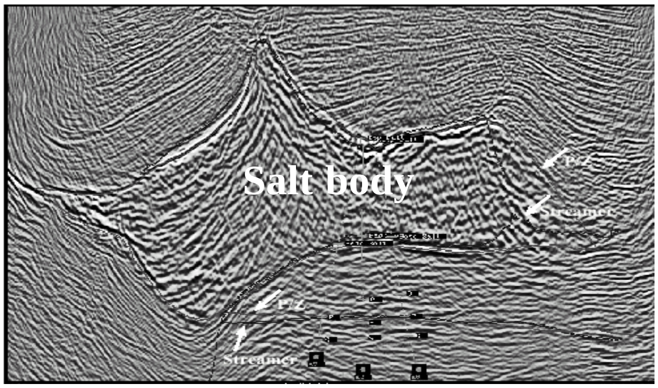

FIG. 4-2. Seismic section showing the salt body of the Mahogany field, offshore Gulf of Mexico (from Kendall and Tollestrup, 1999).

Kendall and Raymer (1999) isolated the converted downgoing wavefield of a VSP dataset acquired through the salt and showed that the salt layer of the Mahogany field was anisotropic (transverse isotropy). They also showed that sediments below the salt return to an isotropic state. In a further investigation (Raymer et al., 1999), they measured Thomsen's **d** parameter using ocean-bottom seismic data and VSP data. A measurement for this parameter in a given layer can be obtained using reflection hyperbolae from the top and bottom of the layer and a vertical velocity obtained from a vertical seismic profile. The P-wave interval velocity, $V_2(P)$ is obtained by conventional Dix's equation on surface seismic data and is compared to the true vertical velocity, V_{p0}, which is known from a check shot or more generally from a VSP. This comparison allows the estimation of the Thomsen **d** parameter (Thomsen, 1986):

$$V_2^2(P) = V_{p0}^2(1 + 2d) \tag{4-1}$$

This method was applied to data from the Mahogany oil field. An average value of **d** = –0.13 was obtained with estimation based on 1500m maximum offset (Raymer et al., 1999).

Apparent anisotropy in Southeast Texas

Sriram et al. (1983), as Raymer et al. (1999) compared vertical velocities of compressional and shear waves (RMS), from a check-shot survey in a well in southeast Texas near the town of Cotulla, to conventional reflection NMO velocities. From the latter measurements, they computed the "apparent horizontal velocity" and the vertical velocity from the check-shot survey. They calculated the ratio of the two velocities that they defined as the apparent anisotropy. For this site, they obtained the following conclusions (after Sriram et al., 1983):

(1) There was no apparent anisotropy for P-wave velocity.
(2) The apparent anisotropy for SH-waves was about 30% (ratio of the NMO velocity over the one obtained from VSP was 1.3) for the first 1000ft below the surface and varies between 10% and 20% below this depth.
(3) The apparent anisotropy for SV waves is around twice as big as for SH waves and averages around 40%.

Anisotropy measurements in sedimentary rocks

Thomsen (1986) gathered numerous published data at that time on anisotropy of sedimentary rocks in order to illustrate his theory on weak elastic anisotropy. He computed the three Thomsen parameters (equations 2-12 and 2-18) for all these examples. We only present some of his results in Table 4-1.

As previously said, transverse isotropy is the most encountered type of anisotropy in nature. Therefore, this is the symmetry we will consider for our synthetic anisotropic model and Thomsen's parameters are a convenient way to quantify the amount of anisotropy for such media. They also help to intuitively understand this type of anisotropy and we will mainly use them to determine it. These measurements provide a valuable insight on a realistic range of exploration for these parameters. It will also help us to verify whether the Thomsen's parameters providing the best fit with the observed travel times are compatible with the local geology.

Table 4-1. Some measurements of the Thomsen's parameters in sedimentary rocks (from Thomsen, 1986).

Sample	V_p***(m/s)***	V_s***(m/s)***	*e*	*d*	*g*	*r* ***(g/cm^3)***
Taylor sandstone	3368	1829	0.11	-0.035	0.255	2.500
Mesaverde mudshale	4529	2703	0.034	0.211	0.046	2.520
Mesaverde immature sandst.	4476	2814	0.097	0.091	0.051	2.500
Mesaverde silty limestone	4972	2899	0.056	-0.003	0.067	2.630
Mesaverde clayshale	3928	2055	0.334	0.730	0.575	2.590
Mesaverde laminated siltst.	4449	2585	0.091	0.565	0.046	2.570
Mesaverde calcerous sandst.	5460	3219	0.000	-0.264	-0.007	2.690
Mesaverde sandstone	3962	2926	0.055	-0.089	0.041	2.87
Mesaverde shale	3383	2438	0.065	0.059	0.071	2.350
Dog Creek shale	1875	826	0.255	0.100	0.345	2.000
Wills Point shale	1058	387	0.215	0.315	0.280	1.800
Cotton Valley shale	4721	2890	0.135	0.205	0.180	2.640
Pierre shale	2074	869	0.110	0.090	0.165	2.250
Green River shale	4167	2432	0.040	0.010	0.030	2.310
Berea sandstone	4206	2664	0.002	0.020	0.005	2.140
Bandera sandstone	3810	2368	0.030	0.045	0.030	2.160
Lance sandstone	5029	2987	-0.005	-0.015	0.005	2.430
Fort Union siltstone	4877	2941	0.045	-0.045	0.040	2.600
Timber Mountain tuff	4846	1856	0.020	-0.030	0.105	2.330

Seismic anisotropy of shales

Johnston and Christensen (1995) investigated the seismic anisotropy of three Devonian-Mississippian shale formations using laboratory velocity measurements as a function of confining pressure. Samples were collected from the Chattagoona Shale of eastern Tennessee, the new Albany Shale of the Illinois basin and the lower Antrim Shale of the Michigan basin. For several samples of shale, they took 2.54-cm-diameter core, parallel, perpendicular and at 45° to bedding. They thoroughly measured seismic velocities for the three different direction of polarization, as well as lengths, weights and diameters of cores to determine sample density. Those measurements allowed them to compute elastic coefficients, as well as Thomsen's parameters. Table 4-2 presents results they obtained for one sample. For cores taken perpendicular to bedding, the distinction V_{sv} - V_{sh} is obviously not used. Table 4-3 presents the corresponding elastic coefficients.

Table 4-2. Laboratory measurements on a sample of anisotropic shale (after Johnston and Christensen, 1995).

VELOCITIES (m/s)

	Perpendicular		45º			Parallel to bedding		
P (Mpa)	V_p	V_s	V_p	V_{sh}	V_{sv}	V_p	V_{sh}	V_{sv}
10	3173	2100	3661	2393	2242	4184	2638	2113
50	3433	2188	3842	2463	2340	4361	2712	2195
100	3598	2257	3982	2527	2409	4489	2774	2268

Those results will allow us to check the relevance of the anisotropy parameters that will be found in the next chapter for the studied dataset. By knowing a realistic range of the values we expect, we also can narrow the search. In the next part the dataset is presented as well as the final results.

Table 4-3. Elastic coefficients and Thomsen's parameters computed from the measurements of Table 4-2 (after Johnston and Christensen, 1995).

Pressure (Mpa)	Elastic coefficients (GPa)					Thomsen's parameters	
P	C_{11}	C_{12}	C_{33}	C_{44}	C_{13}	ε	δ
10	41.75	8.56	24.01	10.58	7.87	0.37	0.18
50	45.36	10.28	28.11	11.45	9.04	0.31	0.14
100	48.06	11.36	30.88	12.20	10.17	0.28	0.13

CHAPTER V

APPLICATION TO A VSP DATASET

This studied dataset was acquired over a mature field that was one of the first oil fields in which oil was found on the flank of the salt dome. The acquisition area is located in the Southwest Louisiana Salt Basin, onshore Gulf of Mexico, USA. Production is from Tertiary sands located between 1900 and 3400 feet of depth (Constance et al., 1999). Overlying shales, the salt dome and the depositional geometry provide the trapping mechanism for hydrocarbon reservoirs. More than 1100 wells were drilled in the area.

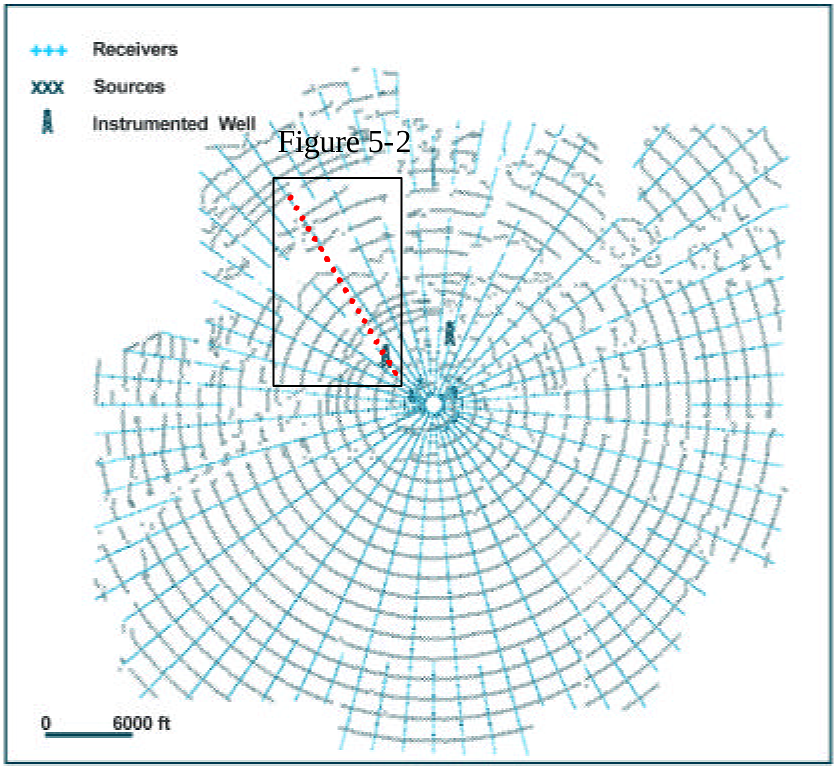

FIG. 5-1. The data acquisition grid (after Constance et al., 1999). The 31 shot gathers that will be used in the next sub-chapter are taken along the northwest trending dotted line. The rectangle is zoomed in Figure 5-2.

Geological background

The salt dome pierced the overlying sediments and nearly reached the surface. The movement of the salt induced a complex faulting system in the surrounding sediments

(Constance et al. 1999). The main sediment formations in the subsurface besides the salt dome include a series of sand and clay, heavy sands and gravels with a small amount of shales and gumbo (a fine silty soil, common in the southern and western United States that forms an unusually sticky mud when wet.). The part of the series lying below includes gumbo with a varying amount of sand, sand and sandy shales. At the base of the series lies a large bed of heaving shale.

Seismic survey

The acquisition scheme is the same for the surface seismic survey and the vertical profiles (Constance et al., 1999). It is made of a radial receiver grid with concentric circular source lines imposed on a topologically flat area (Figure 5-1). Surface seismic sensors are one-component vertical geophones while downhole recorders (65) are three-component geophones (Constance et al., 1999). Seismic sources were simultaneously recorded by the surface spread and by the downhole arrays deployed in two abandoned boreholes (Figure 5-1). The sample rate is of 2 ms. Source depth ranges between 58 and 79 ft (Tzimeas, personal communication). The salt dome is approximately 6000ft wide and 4000ft high in the center of Figure 5-1. A more extensive description of the acquisition parameters can be found in Constance et al. (1999).

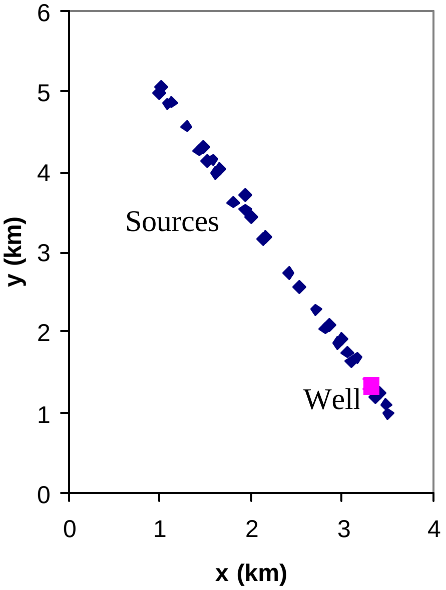

FIG. 5-2. Zoom over the rectangle shown in Figure 5-1 to show the exact positions of the 31 sources and the well.

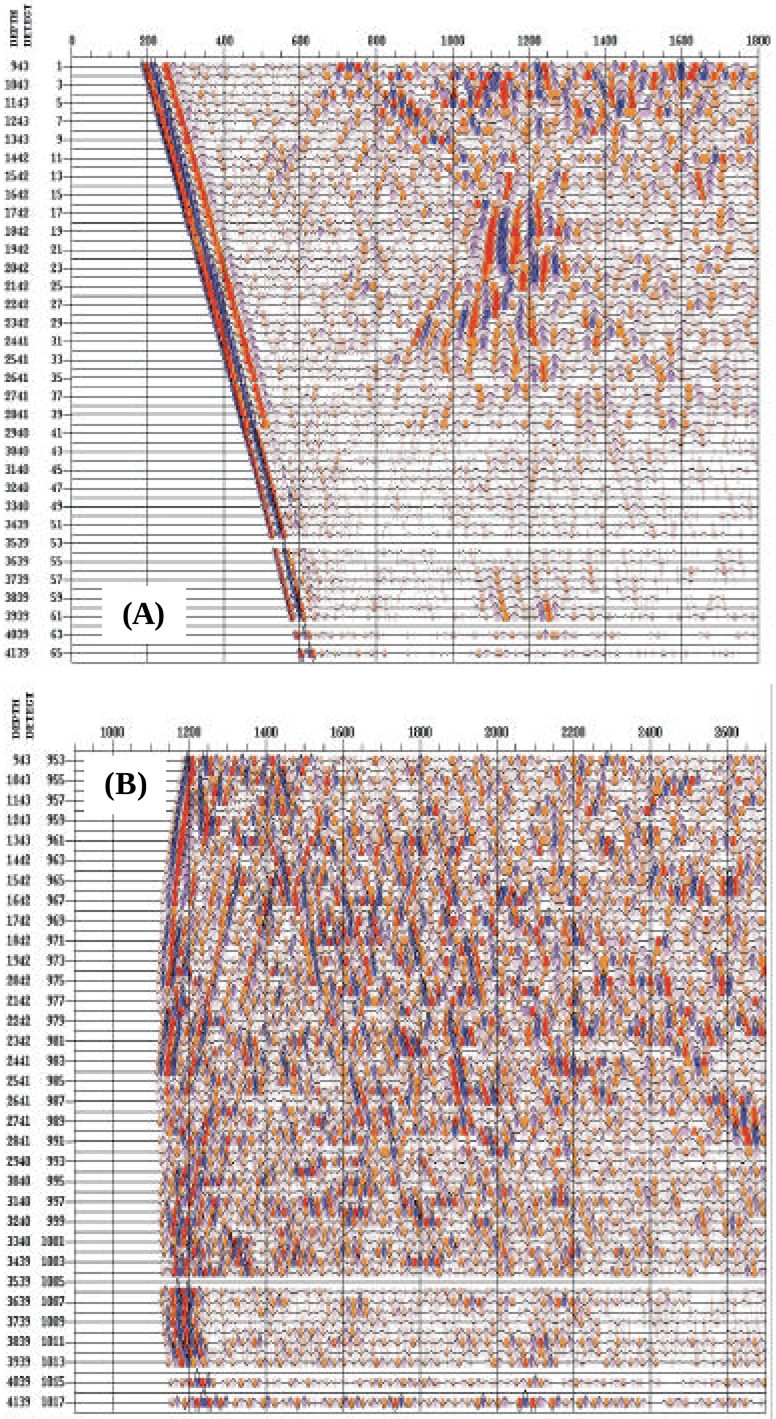

FIG. 5-3. VSP vertical component gathers for nearest (A), intermediate (B) and furthest (C) shot points, along a northwest trending line of Figures 5-1 and 5-2. The vertical axis is the receiver depth (ft) and the horizontal one is time (ms). The second column indicates trace number. Note the linear moveout due to a downgoing wave in (A) and waves nearly traveling horizontally (infinite apparent velocity) in (B).

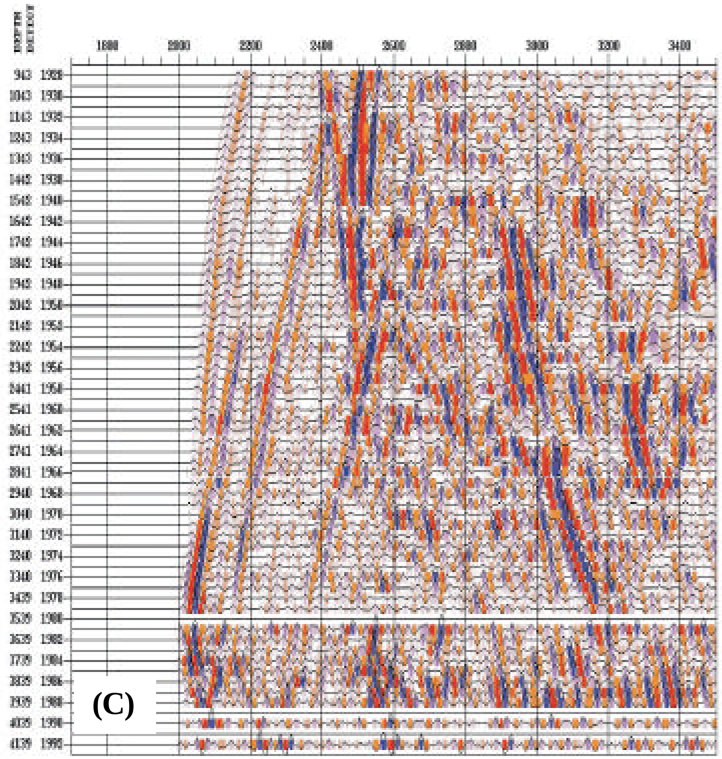

FIG. 5-3. Continued. The moveout is reversed in comparison to shot gather (A) and is characteristic of an up going wave.

A set of 31 shot gather have been chosen along the northwest trending line shown in Figure 5-1. Figure 5-2 enlarges the rectangle around the profile and presents the position of the sources and the well in more detail. The total number of traces is 1992. Figure 5-3 shows the vertical component for nearest (A), intermediate (B) and farthest (C) among the 31 shot gathers of the studied profile (Figure 5-1 and 5-2). The first arrivals observed for the near offset shot gather exhibit a conventional linear moveout, while farther offset VSP exhibit slightly curved negative moveout. The intermediate shot gathers behaves as if waves travel horizontally. The wide range of propagation angle presented by this VSP dataset should allow us to investigate the influence of a possible transversely isotropic behavior of the medium. To do this, we will focus on the first arrival times picked along the profile of Figure 5-2.

The picking of first arrival times has been made using SeisLink™ by automatically detecting the first peak of maximum amplitude shown in (A) in Figure 5-4 (Priest and Tzimeas, personal communication). However, the very first arrival recorded by the receiver is at the onset (point B of Figure 5-4) and not in point (A). Thus, an average onset correction was estimated for each shot gather. The automatically picked times were then decreased by this amount for each shot gather. This indirect picking method is more exact than a direct picking of the onset. Indeed, an amplitude pick is easier to be picked than the emergence of a signal.

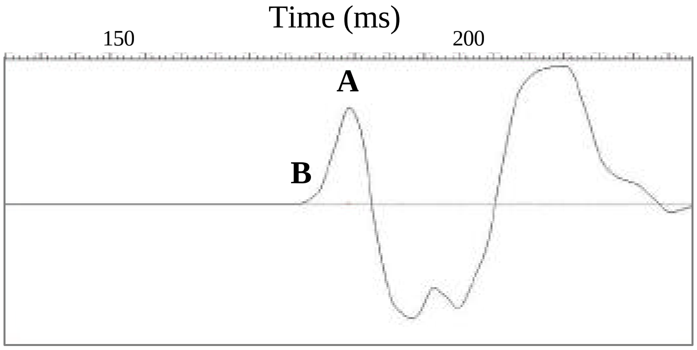

FIG. 5-4. Seismic trace 1 (Figure 5-3A). The first amplitude peak automatically picked with SeisLink™ is shown in (A) and the final arrival time after the onset correction is shown in (B) (after Tzimeas and Priest, personal communication).

Initial velocity model

Before using these first arrival times for our analysis, we had to consider the background information to facilitate the design of a starting model. Some previous work was made on this dataset and some results were available in order to estimate an initial velocity model. Specifically, a three-dimensional velocity model for P-wave velocity has been determined by velocity analysis on surface seismic data (Priest, personal communication). The model had sharp interfaces and had to be simplified prior to any computations with our algorithm. The main characteristics of this velocity model were a velocity generally increasing with depth, a dip of 10 degrees toward the northwest at the well, and then, sediment layers gently becoming horizontal a few kilometers away from the dome. We used this information (the velocity increase with depth, the 10° dip at the well and the horizontal layers at some distance from the salt dome) to constrain the initial model, and ignored other details of the three-dimensional velocity model. This initial structure could be easily simulated using gradients (the method is described in the previous chapter). To simulate the velocity increase with depth, a velocity gradient was also used. This method is widely used to approximate heterogeneity of the subsurface (Popov and Camerlynck, 1996; Miller at al., 1997; Julia et al., 1998; Mitchell, 1998; Bostock, 1999; Hansen et al., 1999;

Muller et al., 2000; Tittgemeyer et al., 2000; Darbyshire et al., 2000; Mereu, 2000; Wang et al., 2000; Dean et al., 2000; among others). This gradient was estimated using a local velocity analysis on the VSP shot gather that is the closest to the well (Tzimeas, personal communication). This profile provided the interval velocities and values for the gradient and the initial velocity (at depth equal zero) were obtained using a linear regression (Figure 5-5). The initial P-wave velocity was 1.779 km/s at the top of the well and the vertical velocity gradient was 0.71 km/s/km. The corresponding P-wave velocity at x and y equal to zero (origin of our axes shown by Figure 5-2) is 1.9615 km/s. This value will be our reference velocity that will be adjusted later to improve the initial model. The resulting velocity model is presented in Figure 5-6. The center of the salt dome is not shown on this figure and is approximately located at -1 km on the horizontal axis. Although it requires some adjustments, this simplified velocity model provided us with the background information necessary to design a model somewhat compatible with the local geology. It also allowed us to identify some parameters that can be varied in order to improve the starting model (these parameters will be presented in the following sections).

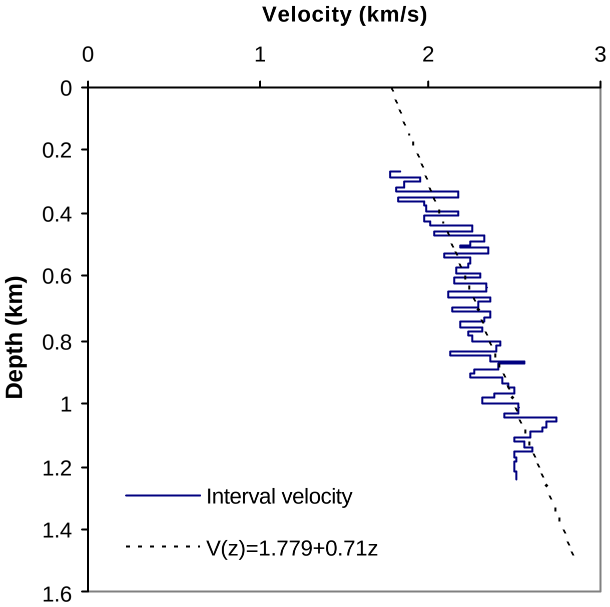

FIG. 5-5. Results of the one-dimensional velocity analysis used to obtain a vertical profile for the interval velocities at the well (Tzimeas, personal communication). This velocity analysis was made using the shot gather that is the closest to the well (not contained in the profile of Figure 5-2). We used this vertical velocity profile to compute the vertical gradient approximating the velocity increase with depth (linear regression). The gradient in depth is 0.71 km/s/km and the P-wave velocity at the top of the well is 1.779 km/s, which corresponds to a velocity of 1.9615 km/s at the origin of axes shown in Figure 5-6.

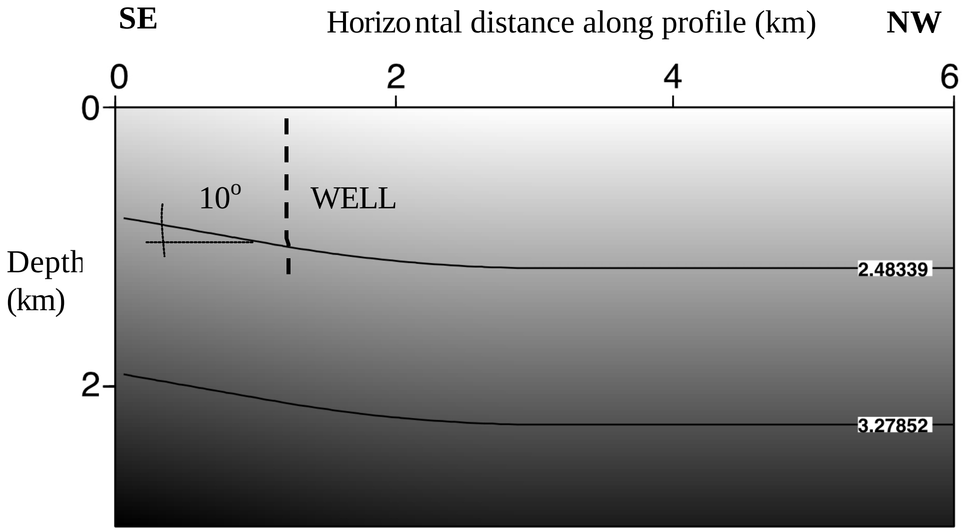

FIG. 5-6. Synthetic velocity model initially used to compute first arrival times with the algorithm by wavefront construction method. The gradient in depth is 0.71 km/s/km. The P-wave velocity at the top of the well is 1.779 km/s, which corresponds to a velocity of 1.9615 km/s at the origin of axes. The dip is of 10 degrees at the well and sediment layers softly become horizontal a few kilometers away from the salt dome in the northwest direction. Plain lines show the constant velocity curves and are labeled in km/s (after Tzimeas and Priest, personal communication).

The earth model class described in the previous chapter requires the knowledge of elastic coefficients a_{ij} and they were computed from the vertical velocity simply by taking the square of it ($a_{33} = C_{33}/r = V_P^2$, equations 2-7 and 2-13). Hence, a good estimation of the ground density was not strictly necessary to establish a model. A dummy value was also attributed to the shear-wave velocity (we only focus on P-wave for isotropic models and quasi-P waves for anisotropic ones).

The method to build the initial model shown in Figure 5-6 has been described in chapter III. Only the layers and the smoothed transition zone are vertical and equations of chapter III are applicable for the y-coordinate, instead of the z-coordinate used to present the multi-gradient method (the gradient change is horizontal in this case). The dip is simulated by the introduction of a horizontal component in the gradient (a or b in equation 3-5). The dip is given by the tangent between horizontal and vertical components of the velocity gradient:

$$\tan(dip) = \frac{horizontal\ \ gradient\ \ component}{vertical\ \ gradient\ \ component}. \qquad (5\text{-}1)$$

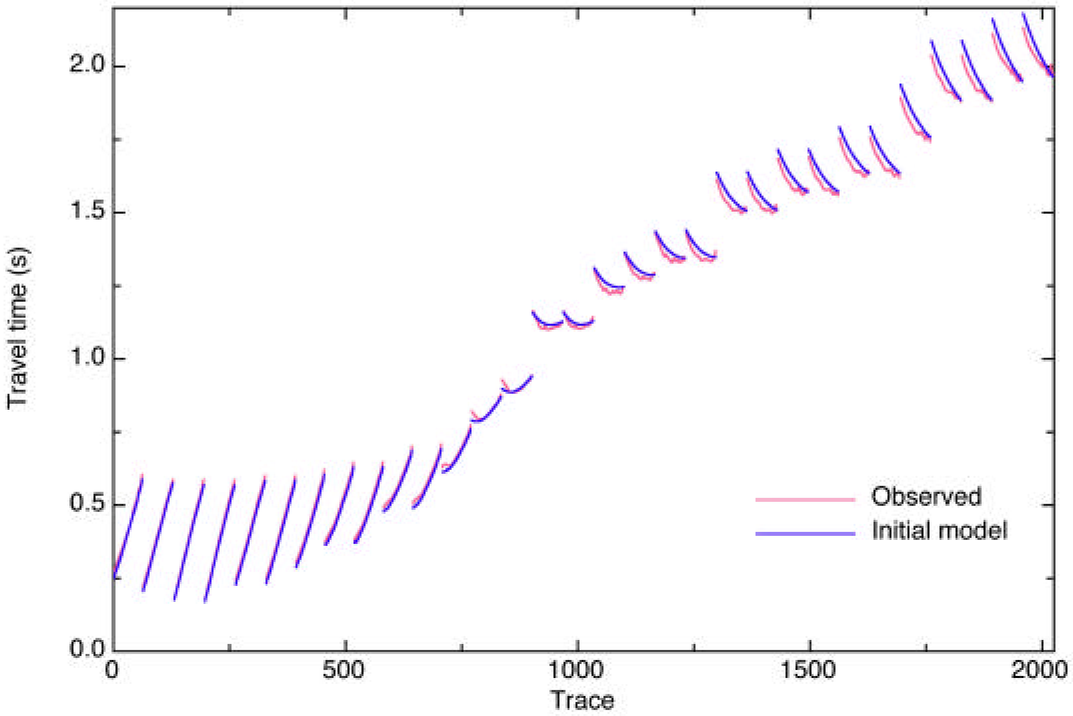

FIG. 5-7. Measured travel times (pink) for the 31 shot gathers taken along the northwest trending profile shown in Figures 5-1 and 5-2, and the ones computed for the synthetic model shown in Figure 5-6 (dark blue). Traces of all shot gathers were arranged in numerical order for display purposes. Individual data points are then simply represented using a sequential trace number: shot gather 1 (Figure 5-3A) from trace 1 to 65; shot gather 2 from trace 66 to 130; and so on. The shot gather exhibiting the smallest source-well offset (and therefore exhibiting the smallest travel times) is the fourth one, starting from the left. The left side of this Figure represents sources that are on the southeast part of the profile shown in Figure 5-1 and 5-2.

Hence, this model can be viewed as a two vertical layer model where the vertical velocity gradient is the same everywhere, but a horizontal component has been introduced only in the left vertical layer to simulate a 10 degree dip. As a result, the horizontal component of the velocity gradient is –0.1252 km/s/km in the left layer (tan(-10º) = -0.1252/0.71, equation 5-1). In Figure 5-6, a large transition zone (2km) between the two vertical layers has been used in order to model a gentle change in slope, as the one exhibited by the three-dimensional velocity model previously computed (Priest, personal communication). This synthetic model has been used to compute first arrival times with the wavefront construction method algorithm. Results are presented in Figure 5-7, where the measured travel times are shown in pink and the computed ones are shown in dark blue. The differences between both times in milliseconds are shown in Figure 5-8. Even though both seem to agree for the 11 near offset shot gathers, the difference become significant as the offset (trace number) increases. To estimate the errors in picking we assume that the model is smooth. Therefore, the small high frequency variations we can observe for consecutive traces provide a rough estimate of error in picking first arrival travel times. The variations are on the order of 4 to 5 ms (Figure 5-8). The time differences are of the order of several tens of milliseconds and therefore can be reduced, even for near offset shot gathers. The errors also vary within one shot gather. Indeed, for the far-offset shot gathers, the errors are small for bottom receivers and high for top ones (bottom receivers are on the right for each shot gather in Figure 5-7 and 5-8). The main idea is to check if these differences can be due to the presence of seismic anisotropy in the geological layers. Two models have been built to reduce the far offset differences in travel times: an isotropic and an anisotropic one.

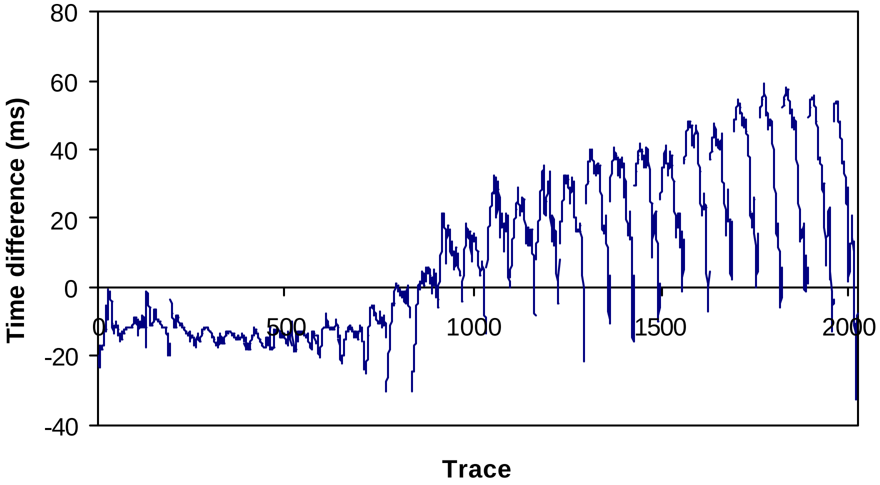

FIG. 5-8. Difference between synthetic travel times and measured travel times for the initial model for the 31 shot gathers of the northwest trending profile of Figures 5-1 and 5-2.

Before explaining the method used to find these models, we need an indicator to quantify the agreement between the synthetic travel times and the measured ones. The average Root Mean Square (RMS) time difference is defined by:

$$\Delta t_{RMS} = \sqrt{\sum_{i=1}^{N} \frac{\left(t_{synth}^{(i)} - t_{real}^{(i)}\right)^2}{N}}, \qquad (5\text{-}2)$$

where N is the total number of traces.

This RMS average time difference will help us to estimate the quality of a synthetic model. Hence, the best synthetic model can be found by means of a simplified inversion using a grid search on relevant parameters (these parameters depend on the model considered and are presented in the following sections). The RMS time difference for the 11 near-offset shot gathers (695 traces) is of 13.7 ms for the initial model. The value for all traces is of 24.3 ms.

Isotropic velocity model

As an alternative to the anisotropic solution presented in the next section, an isotropic model had been sought. Even though the biggest differences between observed and computed travel times are for far-offsets (i.e. trace numbers strictly greater than 695 on Figure 5-7 and 5-8, which exclude the 11 near-offset shot gathers), results for near offsets can also slightly be improved. Those two problems pertaining to near and far offsets were considered independently. This was done by considering a left part on the velocity model, where layers are 10 degree-dipped and with a vertical velocity gradient; and a right part where the vertical velocity gradient is the same that in the left part, but where other parameters such as horizontal velocity gradient or the starting velocity, must be changed to decrease far offset discrepancies. The limit between the two parts is simply the two kilometers wide vertical smoothing transition zone centered at 2.04 km on the horizontal axis of Figure 5-6.

The first task was then to slightly modify the left part of the velocity model to decrease the travel time differences for near-offset. The dip of 10 degree seemed to be a characteristic of the local geology (Tzimeas and Priest, personal communication) and therefore was kept. However, the near-offset shot gather used to estimate the starting velocity at the origin (1.9615 km/s) and the vertical gradient (0.71 km/s/km) is not contained in the profile shown in Figure 5-1 and 5-2. Furthermore, these two parameters could be slightly adjusted without fundamentally changing the velocity model. A grid search was made on these two quantities to obtain the pair providing the minimum RMS time difference for the first 695 traces. Therefore, the first step was to iterate over the starting velocity (at the origin of axes of Figure 5-6) and vertical gradient to find the values providing the minimum RMS time difference for the 11 near-offset shot gathers, the layers remaining horizontal in the northwest part of the profile. Results are shown in Figure 5-9. The minimum near-offset RMS time difference was found for a starting P-wave velocity of 1.905 km/s and a gradient in depth of 0.75 km/s/km. The corresponding near-offset RMS time difference is 3.8 ms (to be compared to 13.7 ms for the initial model).

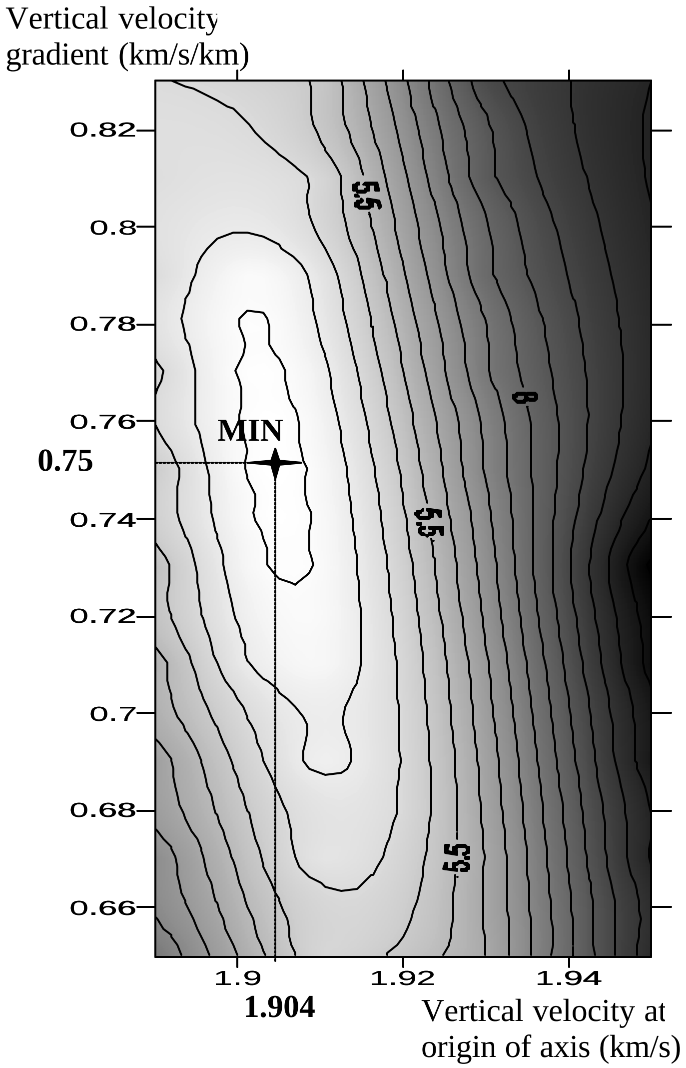

FIG. 5-9. Near offset RMS travel time error as a function of the starting P-wave velocity and vertical gradient. Black color indicates high RMS time difference and white indicates small values. The minimum is found for a starting velocity of 1.905 km/s and a gradient of 0.75 km/s/km.

Once the near-offset RMS time difference was reduced, the second step was to reduce the discrepancies for the remaining traces (far-offset, i.e. trace number greater than 695 on Figure 5-7 and 5-8). A general positive trend can be noticed for the far-offset travel time differences (Figure 5-8). Thus, the computed time is greater than the observed one and the velocity in the right part of the initial model shown in Figure 5-6 must somehow be increased.

With the multi-gradient method described in chapter III, this can be done effectively by adding a positive horizontal component to the velocity gradient, but only in the right vertical layer of Figure 5-6 (the left vertical layer was already optimized, as explained in the above paragraph). As said earlier, the introduction of this horizontal component can be viewed as the introduction of a dip in the simulated horizontal layering. Since the vertical component was given by the previous grid search (Figure 5-9), varying the horizontal component is strictly equivalent to varying the dip (equation 5-1). For this reason and because the idea of a dip is more straightforward to understand than the idea of a horizontal component in the velocity gradient, the dip is the parameter that was chosen for the grid search attempting to decrease the far-offset discrepancies. The RMS time difference was computed for sparse values of the dip ranging from -10º to 10º. As expected, only positive values of the dip decrease the far-offset travel time discrepancies, i.e. the velocity in the left part of the initial model (Figure 5-6) must be increased. Using this multi-gradient approach, the zero dip matching the initial model cannot reduce the far-offset errors whatsoever. As a result, a detailed grid search has only been made for positive values of the dip angle (Figure 5-10). The minimum is for a dip of 4.35 degrees and gives a RMS time difference of 17.8 ms for all the traces (to be compared to 24.3 ms for the initial model). The corresponding RMS time difference for 11 shot gathers close to the well is 4.5 ms. The resulting isotropic velocity model is shown in Figure 5-11 and the difference between measured and computed travel times is the green curve of Figure 5-12.

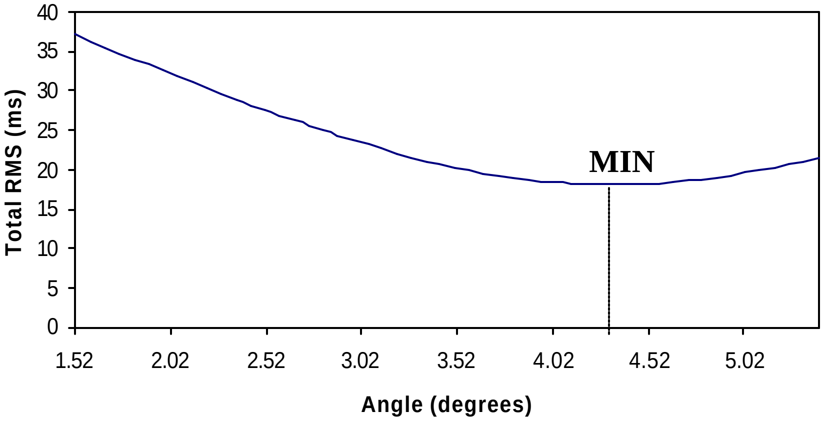

FIG. 5-10. Total RMS time difference as a function of the dip of the second flank of the syncline. The minimum is found for a dip of 4.35 degrees.

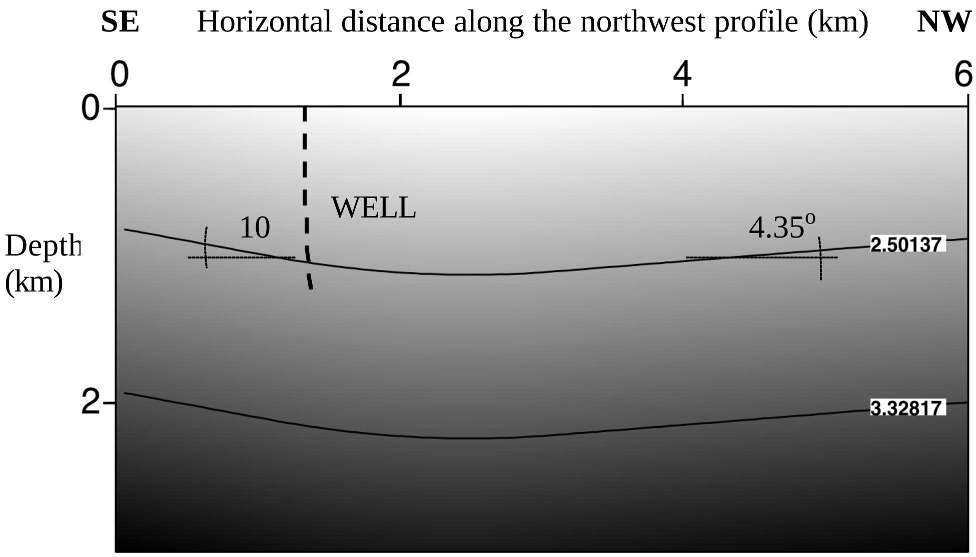

FIG. 5-11. Resulting synthetic isotropic model after iterative processes presented in Figure 5-9 and 5-10. This model is the isotropic model that provided the best fit with measured travel times. Straight lines show the shape of the constant velocity curves and are labeled in km/s

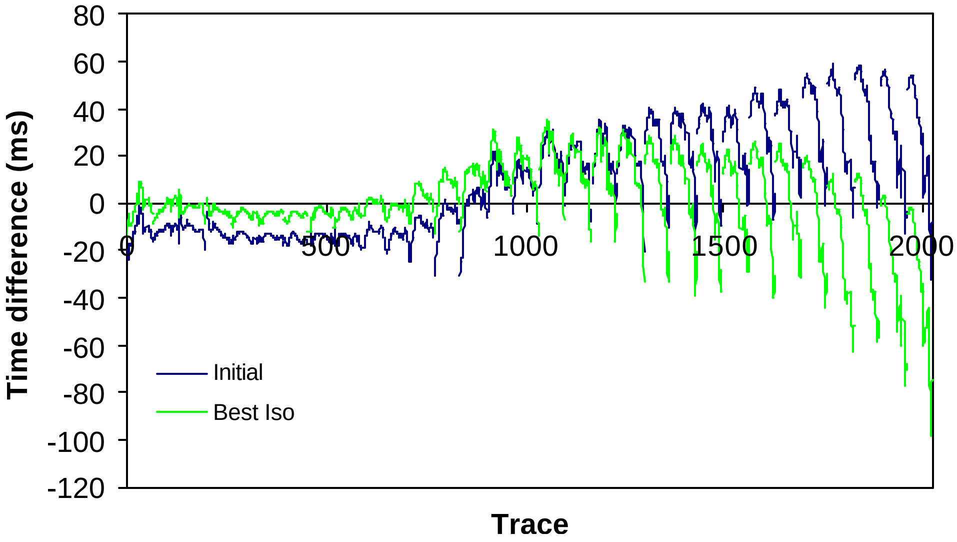

FIG. 5-12. Differences between synthetic and measured travel times for the initial model (blue) and the best isotropic model with a syncline shape (green) presented in Figure 5-11.

Anisotropic velocity model

The approach to find the anisotropic velocity model was slightly different since we wanted to see if the far-offset discrepancies could be explained by anisotropy without changing the structure of the initial velocity model of Figure 5-6. More precisely, the layers in the left part of the model had to remain horizontal. However, for the same reason that leaded us to adjust the starting velocity and the gradient in the isotropic model, the vertical velocity at the origin (Figure 5-6) was re-adjusted, as well as the vertical gradient for the vertical velocity (since the medium is anisotropic, we have to specify the direction when we refer to the velocity). Furthermore, there is no particular reason why the pairs providing the best fit for the isotropic and the anisotropic models would be the same.

Because the type of anisotropy most likely to occur is transverse isotropy, this is the type of symmetry that was considered for our model (see chapter II). As previously explained Thomsen's method (1986) is a good way to parametrize such a model and is especially suitable for a grid search. Hence, to find the model providing the minimum RMS time difference, we made the anisotropy of the model vary by means of Thomsen's parameters e and d (equations 2-12 and 2-18). Thomsen's parameters e and d are constant throughout the model. As previously said, we only consider P-wave propagation and thus we only considered the parameters directly related to it (e, d and the vertical P-wave velocity) and ignoring those related to the propagation of shear-waves (g and the vertical S-wave velocity).

The grid search therefore included four parameters: e, d, the vertical P-wave velocity at the origin, and the vertical gradient of the vertical P-wave velocity. To reduce computation times, parameters providing the best fit were searched by pair: e and d varying with vertical velocity and gradient kept constant on one hand; and vertical velocity and gradient varying with e and d kept constant on the other hand. At first e and d varied whereas we retained the vertical velocity and gradient of the initial model of Figure 5-6 (respectively 1.9615 km/s and 0.71 km/s/km). Once the best pair (e, d) was found, we adjusted the starting P-wave vertical velocity as well as the gradient in depth. When the best pair of velocity and gradient values is found, we adjusted previous values e and d to find the best match; and so on until no significant improvement can be done. As a result, the best vertical velocity was found to be 1.9437 km/s, compared to 1.9615 km/s for the initial model of Figure 5-6. The depth gradient remained the same, i.e., 0.71 km/s/km. Figure 5-13 presents the RMS time differences for several values of e and d, for the best velocity and gradient value. The minimum occurred for $\varepsilon = 0.055$ and $\delta =$ -

0.115. The resulting differences between computed and measured travel times for the 31 shot gathers are given in Figure 5-14. The RMS time difference for the 11 shot gathers close to the well is 7.4 ms and the total RMS time difference is 11.9 ms.

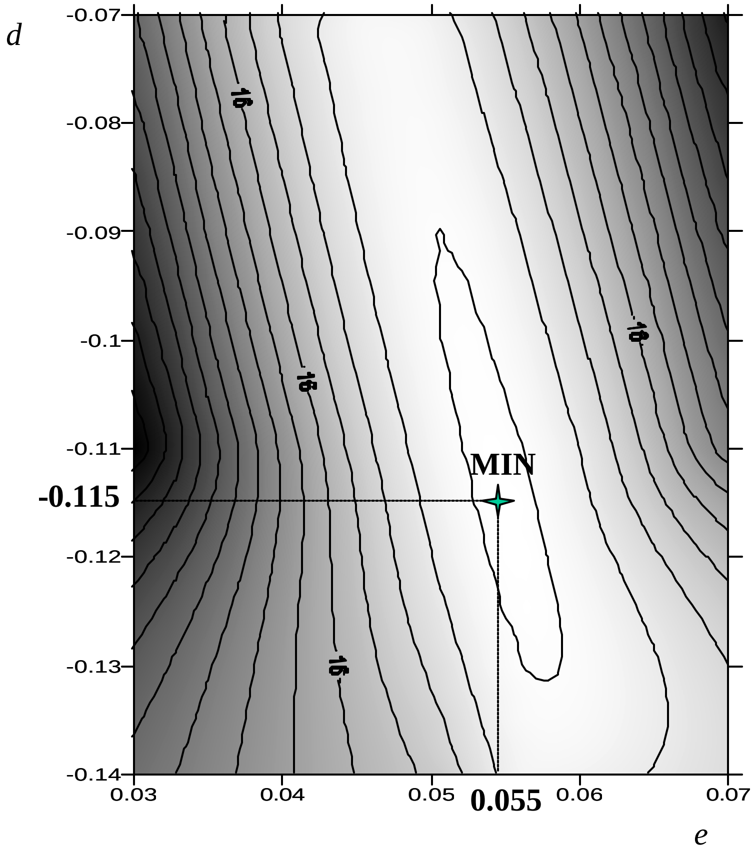

FIG. 5-13. Total RMS time difference for different values of the couple (*e*, *d*). The vertical P-wave velocity at the origin is 1.9437 km/s and the corresponding gradient is 0.71 km/s/km. High RMS is shown in black and low RMS in white. The minimum was found for *e* = 0.055 and *d* = -0.115.

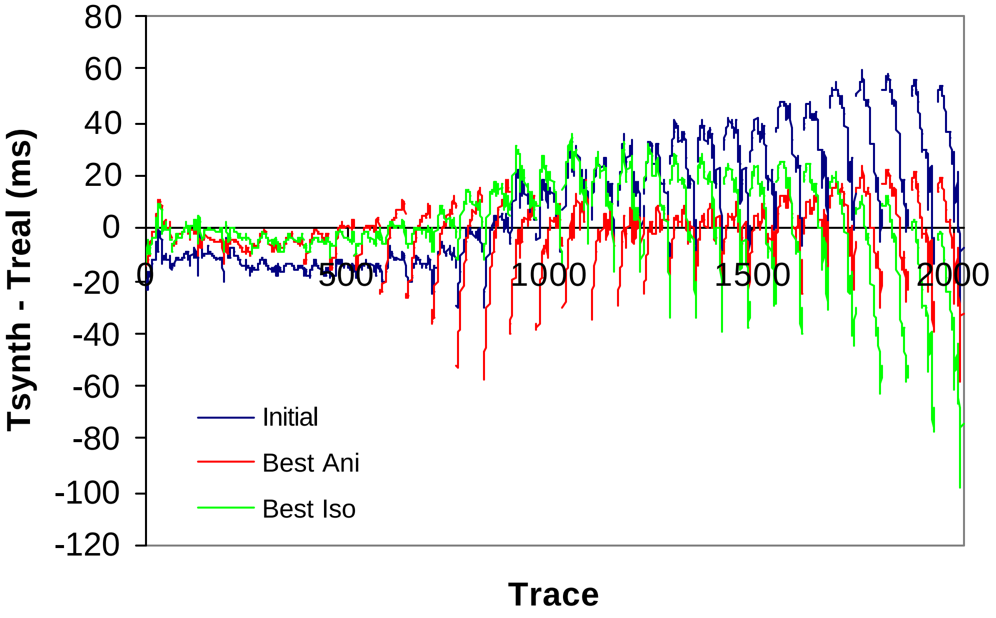

FIG. 5-14. Difference between computed travel times and measured ones for the initial model (dark blue), the syncline isotropic model (green) and for the anisotropic model giving the minimum RMS time difference (red). For the anisotropic model, the starting velocity at coordinates is 1.9437 km/s, the gradient in depth is 0.71 km/s/km, e = 0.055 and d = -0.115. The near offset RMS is 7.4 ms and the total one is 11.9 ms.

Discussion

Table 5-1 summarizes the results obtained for the different synthetic models. The anisotropic model parameters have been determined using the total RMS time difference. As a result, the isotropic model has a better fit for near-offset travel times than the anisotropic model, but the latter has a better fit when the total number of traces is taken into account. For both proposed models, isotropic and anisotropic, a compromise has been made between a good fit for near-offset and a good fit for far-offset. For instance, an anisotropic model having a better fit for near-offset travel times (near RMS < 4 ms) can be found using the same scanning method. However, the total RMS time difference would have been greater than 11.9 ms.

Even though the errors of the isotropic syncline model for near-offset shot gathers are reasonable (4.5 ms), they are still large for far-offset shot gathers. However, the total RMS time difference has been reduced by 27% in comparison to the initial model and one might think that the syncline shape of the subsurface layers could explain the far-offset errors, but it is not compatible with the background information on the geology (Tzimeas and Priest, personal communication).

Table 5-1. Results obtained and main characteristics of the three different synthetic models. Velocities are in km/s, depth gradients in km/s/km and RMS time in ms.

Model	Vpv(0,0,58ft)	Z gradient	ε	δ	Near RMS	Total RMS	Shape
Initial	1.9615	0.71	0.0	0.0	13.7	24.3	initial
Isotropic	1.905	0.75	0.0	0.0	4.5	17.8	syncline
Anisotropic	1.9437	0.71	0.055	-0.115	7.4	11.9	initial

The anisotropic velocity model reduces the total RMS time difference by 51% in comparison to the initial model. Therefore, the introduction of anisotropy helps to reduce the far offset errors even when one keeps the same structure for the vertical velocity as the initial velocity model. The Thomsen’s parameters providing the minimum error are $e = 0.055$ and $d = -0.115$. The resulting amount of anisotropy (define by the difference between the maximum and the minimum velocity of the group velocity surface) is 6.9%. This result confirms the weak elastic anisotropy assumption we implicitly made with the use of Thomsen’s parameters. In the brief study on anisotropic measurement presented in chapter IV, the most similar sample, as far as the seismic anisotropy is concerned is the Mesaverde sandstone (Table 4-1). For this sample, $e = 0.055$ and $d = -0.089$ (Lin, 1985). The geological layers of the studied field only partially contain sandstone. Even though the anisotropic model presents lower errors than isotropic models, they remain quite high. The sample rate for the VSP dataset is 2 ms. An average difference of 11.9 ms between computed travel times and measured ones represents around 6 samples which is not negligible. The small variations for near-offset traces could probably be reduced by introducing more detail in the proposed synthetic model. This could be done by building another class in the *EarthModel* class hierarchy, where the model would be defined by a grid of cells where the elastic properties are constant. The model can be smoothed using cubic spline. Models defined analytically do not allow the same flexibility but involve small computation times. For far offset traces, as one can see on Figure 5-12, the introduction of anisotropy did not reduce the variations of the time difference within a shot gather. The difference is positive for top receivers and negative for bottom receivers. It is the opposite for mid-offset shot gathers (around trace number 1000) discrepancies are negative for top receivers and positive for bottom ones. To propose an explanation to this phenomenon, we need to visualize ray paths for the corresponding source-receiver pairs. Figure 5-15 shows travel paths of six different rays traveling in the anisotropic model. Red, blue and green rays are traced from the far, mid and near offset sources respectively. Plain rays arrive at the deepest receiver in the well and dashed rays arrive at the shallowest receiver placed in the well. Results of Figure 5-14 show us that the time difference is negative (synthetic time greater than observed time) for the plain blue ray and the red dashed ray; and that this difference is positive (synthetic time smaller than observed time) for the dashed blue ray and the plain red ray. Hence, to solve these discrepancies, one could slightly increase the velocity in a region located at intermediate depths and offsets (as shown on Figure 5-15) and decrease it above and below.

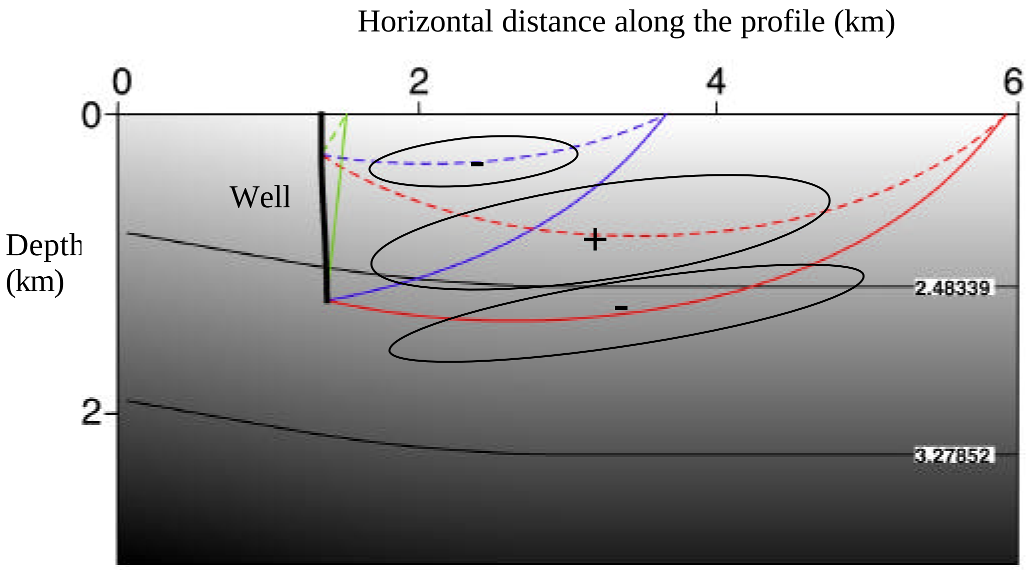

FIG. 5-15. Six different ray paths computed in the anisotropic velocity model. Red, blue and green rays pertain to far, mid and near offset sources respectively. Plain rays reach the deepest receiver placed inside the well and dashed rays the shallowest. The proposed solution to reduce the remaining time differences is to slightly decrease the velocity in a region located at intermediate depths and offsets and to increase it in the surrounding regions.

CHAPTER VI

CONCLUSION

Wavefront construction methods appear to be fast and robust ray tracing techniques, even for complex anisotropic three-dimensional velocity models. The C++ object oriented programming approach is a powerful tool to develop such algorithms, providing in particular flexibility in the implementation of new components. The analytical solution proposed here to program new earth model classes involved little algebra and allowed the modeling of realistic anisotropic models. In particular, it allowed the coding of multi-gradient smooth anisotropic models. This can be used to simulate a subsurface with a vertical gradient, with a dip or even with several dip variations. This method can also be used to simulate multi-layered anisotropic velocity models.

The new earth model classes have been used to estimate the amount of anisotropy in the studied VSP dataset. The initial isotropic velocity model produces big errors between measured and computed first arrival times, especially for far offset shot gathers. Two approaches were used to reduce the discrepancies: isotropic and transversely isotropic. The isotropic approach requires to change the basic structure of the initial model to match the measured time for long offsets. An isotropic model keeping the same structure as the initial velocity model given by the background information cannot reduce the errors whatsoever. As a result, an isotropic syncline model reduces subsequently the RMS average time difference by 27%. However, this model is not compatible with the information gathered on the local subsurface. In contrast, the anisotropic velocity model keeps the basic structure and reduces the RMS time difference by 51% in comparison to the initial isotropic model. The model is transverse isotropic and the anisotropy is constant throughout the model. It has been simulated by means of Thomsen's parameters d and e. Values providing the best fit are $e = 0.055$ and $d = -0.115$. The corresponding amount of anisotropy is 6.9%, which is consistent with observations made by Thomsen (1986) that in most cases, the anisotropy is weak. The values of the Thomsen's parameters are also very close to those found by Lin (1985) for a Mesaverde Sandstone sample. Even though this anisotropic model offers a better fit with measured travel times, discrepancies are still not negligible. Indeed, the corresponding RMS time difference is 11.9 ms. In particular, some variations in discrepancies are observed within each shot gather for far offset. Top receivers exhibit positive differences (synthetic travel times higher than measured ones) and bottom receivers exhibit negative time differences. The opposite phenomenon is observed for mid-offset shot gathers. The anisotropic velocity model does not explain these discrepancies. Additional testing, such as tomography or inversion would be required to further reduce them. Besides, only one northwest trending profile has been considered and the study of a larger volume within the Vinton VSP dataset could be enlightening.

Currently, the C++ ray-tracing algorithm only allows simulation of first arrival times. However, the coding of procedures allowing amplitude computation is being performed and will soon be operational. This will allow subsequent analysis of amplitude data on complex dataset such as the one studied. Furthermore this will allow the computation of synthetic seismograms that could be compared to the measured ones. Another subsequent development could be the design of a new earth model classes simulating more complex heterogeneous anisotropic models by mean of a three-dimensional grid smoothed by cubic splines.

REFERENCES

Aki, K. and Richards, P., 1980, Quantitative seismology. Theory and methods: W. H. Freeman and Co.

Alford, R.M., Lynn, H.B. and Thomsen, L.A., 1989, Seismic surveying technique for the detection of azimuthal variations in the earth's subsurface: United States Patent, 4.817.061.

An, P., Jula, A., Rus, S., Saunders, S., Smith, T., Tanase, G., Thomas, N., Amato, N., and Rauchwerger, L, 2000, STAPL: An adaptive, generic parallel C++ library: Proc. of the International Workshop on Advanced Compiler Technology for High Performance and Embedded Processors (IWACT), Bucharest, Romania.

Babich, V., 1961, Ray method for the computation of the intensity of wave fronts in elastic inhomogeneous anisotropic medium: Problems of the Dynamic Theory of Propagation of Seismic Waves, **5**, 36-46, Leningrad University Press, Leningrad (in Russian).

Bleistein, N., 1984, Mathematical methods for wave phenomena: Academic Press.

Bostock, M, 1999, Seismic waves converted from velocity gradient anomalies in the Earth's upper mantle: Geophys. J. Int., **138**(3), 747-756.

Camp, W.K. and McGuire, D., 1997, Mahogany Field, a subsalt legend: A tale of technology, timing and tenacity, offshore Gulf of Mexico: Issue of the HGS Bulletin, http://www.hgs.org/artcpics/mahog1097.htm.

Carlson, R.L. and Christensen, N.I., 1977, Velocity anisotropy and physical properties of deep-sea sediments from the western South Atlantic: Initial reports of the Deep Sea Drilling Project, **39**, 555-559.

Cervený, V., 1972, Seismic rays and ray Intensities in inhomogeneous anisotropic media: Geophys. J. R. Astr. Soc., **29**, 1-13.

Cervený, V., 1985, The application of ray tracing to the propagation of shear waves in complex media: Seismic shear waves, part A: Theory, edited by G.P. Dohr, *in* Handbook of geophysical exploration, Section 1: Seismic exploration, 15A, edited by Helbig, K., and Treitel, S.: Geophysical Press, 1-124.

Cervený, V., 2001, Seismic ray theory: Cambridge University Press.

Cervený, V., Molotkov, I., and Pšencik, I., 1977, Ray method in seismology: Univ. Karlova, Praha.

Constance, P.E., Holland, M.B., Roche, S.L., Bicquart, P., Bryans, B., Gelinsky, S., Ralph, J.G., and Bloor, R.I., 1999, Simultaneous acquisition of 3-D surface seismic data and 3-C, 3-D VSP Data: SEG 1999 Expanded Abstracts, ref. BH/RP 4.5 (from CD).

Crampin, S., 1981, A review of wave motion in anisotropic and cracked elastic media: Wave Motion **3**, 343-391.

Crampin, S., 1984, An introduction to wave propagation in anisotropic media: Geophys. J. R. Astr. Soc., **76**, 17-28.

Darbyshire, F., Priestley, K., White R., Stefansson, R., Gudmundsson, G., and Jakobsdottir, S., 2000, Crustal structure of the central and northern Iceland from analysis of teleseimic receiver functions: Geophys. J. Int., **143**(1), 163-184.

Dean, S., Minshull, T., Whitmarsh, R., and Louden, K., 2000, Deep structure of the ocean-continent transition in the southern Iberia Abyssal Plain from seismic refraction profiles: J. of Geophys. Res., **105**(B3), 5859-5885.

Gajewski, D., and Pšencik, I., 1987, Computation of high-frequency seismic wavefields in 3-D laterally inhomogeneous anisotropic media: Geophys. J. Astr. Soc., **91**, 383-411.

Gibson, R.L., 2000, Ray tracing by wavefront construction for anisotropic media: SEG Expanded Abstracts, ref. ST4.5 (from CD).

Gibson, R.L., Sena, A.G. and Toksöz, M.N., 1991, Paraxial ray tracing in 3D inhomogeneous, anisotropic media: Geophysical Prospecting, **39**, 473-504.

Godfrey, N., Christensen, N., and Okaya, D., 2000, Anisotropy of schists: Contribution of crustal anisotropy to active source seismic experiments and shear-wave splitting observations: J. of Geophys. Res., **105**(B12), 27991-28007.

Hansen, T., Singh, S., and Jacobsen, B., 1999, Sensivity of seismic wide-angle wavefield and first arrival times to fine scale crustal structure and Moho topography: Geophys. Res. Letters, **26**(16), 2573-2576.

Hilterman, F., Sherwood, J.W., Schellhorn, R., Bankhead, B. and Devault, B., 1998, Identification of lithology in the Gulf of Mexico: The Leading Edge, **17**, 215-218, 220-222.

Johnston, J.E. and Christensen, N.I., 1995, Seismic anisotropy of shales: J. of Geophys. Res., **100**(B4), 5991-6003.

Julia, J., Vila, J., and Macia, R, 1998, The receiver structure beneath the Ebro Basin, Iberian Peninsula: Bulletin of the Seis. Soc. of America, **88**(6), 1538-1547.

Kay, I., Sol, S., Kendall, J., Thomson, C., White, D., Asudeh, I., Roberts, B., and Francis, D., 1999, Shear-wave splitting observations in the Archean craton of western superior: Geophys. Res. Letters, **26**(17), 2669-2672.

Kendall, R.R and Raymer, D.G., 1999, Processing and interpretation of VSP data to determine salt anisotropy – Mahogany field, Gulf of Mexico: EAGE 61st Conference and Technical Exhibition, Helsinki Finland.

Kendall, R.R. and Tollestrup, A.K., 1999, Multicomponent processing and interpretation: Mahogany Field, Gulf of Mexico: SEG meeting abstract, Amoco, http://www.cseg.org/events/meetings/abstracts/1999/ewe_ch1.pdf.

Lambaré, G., Lucio, P., and Hanyga, A., 1996, Two-dimensional multivalued traveltime and amplitude maps by uniform sampling of a ray field: Geophys. J. Int., **125**, 584-598.

Lin, W., 1985, Ultrasonic velocities and dynamic elastic moduli of Mesaverde rock: Lawrence Livermore National Laboratory Report 20273, rev. 1.

Mereu, R., 2000, The effect of small random crustal reflectors on the complexity of Pg and PmP coda: Physics of the Earth and Planetary Interiors, **120**(3), 183-199.

Miller, K., Keller, G., Gridley, J., Luetgert, J., Mooney, W., and Thybo, H., 1997, Crustal structure along the west flank of the Cascades, western Washington: J. of Geophys. Res., **102**(B8), 17857-17873.

Mitchell, B., Baqer, S., Akinci, A., and Cong, L., 1998, Lg Coda Q in Australia and its relation to crustal structure and evolution: Pure and Applied Geophysics, **153**(2-4), 639-653.

Moser, T., 1991, Shortest path calculation of seismic rays: Geophysics, **56**, 59-67.

Muller, M., Minshull, T., and White, R., 2000, Crustal structure of the Southwest Indian Ridge at the Atlantis II Fracture Zone: J. of Geophys. Res., **105**(B11), 25809-25828.

Papadimitriou, P., Kaviris, G., and Makropoulos, K., 1999, Evidence of shear-wave splitting in the eastern Corinthian Gulf (Greece): Physics of the Earth and Planetary Interiors, **114**, 3-13.

Pleneflish, T., Klinge, K., and Kind, R., 2001, Upper mantle anisotropy at the transition zone of the Saxothuringicum and Moldanubicum in Southeast Germany revealed by shear-wave splitting: Geophys. J. Internat., **144**, 309-319.

Popov, M., and Camerlynck, C., 1996, Second term of the ray series and validity of the ray theory, J. of Geophys. Res., **101**(B1), 817-826.

Raymer, D. G. and Kendall, J.M., 1998, Seismic anisotropy in salt structures due to preferred crystal orientation: La Revue de l'IFP, **53**, 35-43.

Raymer, D.G., Kendall, J.M., and Beaudoin, G.J., 1999, Measurements of salt anisotropy: calculating Thomsen's δ parameter in real and synthetic data: Proceedings of 69th Ann. Mtg., Soc. Explr. Geophys., Expanded Abstracts, 1596-1600.

Schildt, H., 1998, C++: The complete reference (third edition), McGraw-Hill.

Shuck, E.L., 1991, Azimuthal anisotropy analysis from shear VSPs: Geophys. J. Int., **107**, 639-647.

Sriram, K.P. et al., 1983, Velocity anisotropy of seismic waves; field observations: SEG Expanded Abstracts, 53rd annual meeting, 1, 596-598.

Stevens, A., and Walnum, C., 2000, Standard C++ bible: IDG Books Worldwide, Inc.

Stroustrup, B., 1997, The C++ programming language (third edition): Addison-Wesley.

Thomsen, L.A., 1986, Weak elastic anisotropy: Geophysics, **51**, 1954-1966.

Tittgemeyer, M., Wenzel, F., and Fuchs, K., 2000, On the nature of Pn: J. of Geophys. Res., **105**(B7), 16173-16180.

Van Trier, J., and Symes, W., 1991, Upwind finite-difference calculation of traveltimes: Geophysics, **56**, 812-821.

Vidale, J., 1990, Finite-difference calculation of travel times in three dimensions: Geophysics, **64**, 1912-1919.

Vinje, V., Iversen, E., and Gjøystdal, H., 1993, Traveltime and amplitude estimation using wavefront construction: Geophysics, **58**, 1157-1166.

Wang, Y., Takenaka, H., and Furumura, T., 2000, Effect of vertical velocity gradient on ground motion in a sediment-filled basin due to incident SV-wave: Earth Planets and Space, **52**(1), 13-24.

Wetzel, A., 1987, Sedimentological significance of strain and sonic velocity anisotropy in fine-grained turbiditic and hemipelagic deep-sea sediments – An example from the Mississippi fan: Marine Geology, **74**, 191-207.

Winterstein, D.F., 1986, Anisotropy effects in P-wave and SH-wave stacking velocities contain information on lithology: Geophysics, **51**, 661-672.

Zhang, J., and Toksöz, M., 1998, Nonlinear refraction traveltime tomography: Geophysics, **63**, 1726-1737.

APPENDIX

The derivatives of elastic coefficients a_{ij} are also required by ray-tracing system (2-11). Their analytical expression is straightforward in the case of a single gradient model (equations 3-9). However, they are more tedious to derive for the multi-gradient model, especially in the smooth transition zone. Equation (3-11a) gives the following expressions for the derivatives of elastic coefficients a_{ij} with respect to spatial coordinates, in layer n outside the smoothed transition zone (Figure 3-10):

$$\partial A_{ij}^{(n)}(x,y,z)/\partial x = 2w_{ij}a\left\{\sqrt{a_{ij}^{(n-1)}} + w_{ij}\left[ax+by+g^{(n)}\left(z-z^{(n-1)}\right)\right]\right\},$$
$$\partial A_{ij}^{(n)}(x,y,z)/\partial y = 2w_{ij}b\left\{\sqrt{a_{ij}^{(n-1)}} + w_{ij}\left[ax+by+g^{(n)}\left(z-z^{(n-1)}\right)\right]\right\}, \qquad \text{(A-1)}$$

and

$$\partial A_{ij}^{(n)}(x,y,z)/\partial z = 2w_{ij}g^{(n)}\left\{\sqrt{a_{ij}^{(n-1)}} + w_{ij}\left[ax+by+g^{(n)}\left(z-z^{(n-1)}\right)\right]\right\}.$$

Inside the smoothing transition zone around an interface at depth $z^{(n-1)}$, these derivatives are given by:

$$\frac{\partial A_{ij}^{smooth}}{\partial x}(x,y,z) = \frac{\partial s_{ij}^{(1)}}{\partial x}z^5 + \frac{\partial s_{ij}^{(2)}}{\partial x}z^4 + \frac{\partial s_{ij}^{(3)}}{\partial x}z^3 + \frac{\partial s_{ij}^{(4)}}{\partial x}z^2 + \frac{\partial s_{ij}^{(5)}}{\partial x}z + \frac{\partial s_{ij}^{(6)}}{\partial x},$$
$$\frac{\partial A_{ij}^{smooth}}{\partial y}(x,y,z) = \frac{\partial s_{ij}^{(1)}}{\partial y}z^5 + \frac{\partial s_{ij}^{(2)}}{\partial y}z^4 + \frac{\partial s_{ij}^{(3)}}{\partial y}z^3 + \frac{\partial s_{ij}^{(4)}}{\partial y}z^2 + \frac{\partial s_{ij}^{(5)}}{\partial y}z + \frac{\partial s_{ij}^{(6)}}{\partial y}, \qquad \text{(A-2)}$$
$$\frac{\partial A_{ij}^{smooth}}{\partial z}(x,y,z) = 5s_{ij}^{(1)}z^4 + 4s_{ij}^{(2)}z^3 + 3s_{ij}^{(3)}z^2 + 2s_{ij}^{(4)}z + s_{ij}^{(5)}.$$

Coefficients $s_{ij}^{(1->6)}$ are given by the continuity of elastic coefficients on the top and bottom of the smoothing transition zone (equations 3-14 and 3-15):

$$\begin{pmatrix} s_{ij}^{(1)} \\ s_{ij}^{(2)} \\ s_{ij}^{(3)} \\ s_{ij}^{(4)} \\ s_{ij}^{(5)} \\ s_{ij}^{(6)} \end{pmatrix} = \begin{pmatrix} z_1^5 & z_1^4 & z_1^3 & z_1^2 & z_1 & 1 \\ z_2^5 & z_2^4 & z_2^3 & z_2^2 & z_2 & 1 \\ 5z_1^4 & 4z_1^3 & 3z_1^2 & 2z_1 & 1 & 0 \\ 5z_2^4 & 4z_2^3 & 3z_2^2 & 2z_2 & 1 & 0 \\ 20z_1^3 & 12z_1^2 & 6z_1 & 2 & 0 & 0 \\ 20z_2^3 & 12z_2^2 & 6z_2 & 2 & 0 & 0 \end{pmatrix}^{-1} \begin{pmatrix} A_{ij}^{(n-1)}\big|_{top} \\ A_{ij}^{(n)}\big|_{bottom} \\ \partial A_{ij}^{(n-1)}/\partial z\big|_{top} \\ \partial A_{ij}^{(n)}/\partial z\big|_{bottom} \\ \partial^2 A_{ij}^{(n-1)}/\partial z^2\big|_{top} \\ \partial^2 A_{ij}^{(n)}/\partial z^2\big|_{bottom} \end{pmatrix}, \qquad \text{(A-3)}$$

where

$$\begin{aligned}
&A_{ij}^{(n-1)}\Big|_{top} = \left\{\sqrt{a_{ij}^{(n-1)}} + w_{ij}\left[ax + by + g^{(n-1)}\left(z^{(n-1)} - z^{(n-2)} - \Delta z/2\right)\right]\right\}^2, \\
&A_{ij}^{(n)}\Big|_{bottom} = \left\{\sqrt{a_{ij}^{(n)}} + w_{ij}\left[ax + by + g^{(n)}\,\Delta z/2\right]\right\}^2, \\
&\partial A_{ij}^{(n-1)}\Big/\partial z\Big|_{top} = 2w_{ij}g^{(n-1)}\left\{\sqrt{a_{ij}^{(n-1)}} + w_{ij}\left[ax + by + g^{(n-1)}\left(z^{(n-1)} - z^{(n-2)} - \Delta z/2\right)\right]\right\}, \\
&\partial A_{ij}^{(n)}\Big/\partial z\Big|_{bottom} = 2w_{ij}g^{(n)}\left\{\sqrt{a_{ij}^{(n)}} + w_{ij}\left[ax + by + g^{(n)}\,\Delta z/2\right]\right\}, \\
&\partial^2 A_{ij}^{(n-1)}\Big/\partial z^2\Big|_{top} = 2\left(w_{ij}g^{(n-1)}\right)^2, \\
&\partial^2 A_{ij}^{(n)}\Big/\partial z^2\Big|_{bottom} = 2\left(w_{ij}g^{(n)}\right)^2, \\
&z_1 = z^{(n-1)} - \Delta z/2, \\
&z_2 = z^{(n-1)} + \Delta z/2,
\end{aligned} \tag{A-4}$$

with Δz the thickness of the transition zone.

Hence, derivatives of coefficients $s_{ij}^{(1->6)}$ are given by:

$$\begin{pmatrix} \partial s_{ij}^{(1)}\big/\partial x \\ \partial s_{ij}^{(2)}\big/\partial x \\ \partial s_{ij}^{(3)}\big/\partial x \\ \partial s_{ij}^{(4)}\big/\partial x \\ \partial s_{ij}^{(5)}\big/\partial x \\ \partial s_{ij}^{(6)}\big/\partial x \end{pmatrix} = Z^{-1}\begin{pmatrix} 2w_{ij}a\left\{\sqrt{a_{ij}^{(n-1)}} + w_{ij}\left[ax + by + g^{(n-1)}\left(z^{(n-1)} - z^{(n-2)} - \Delta z/2\right)\right]\right\} \\ 2w_{ij}a\left\{\sqrt{a_{ij}^{(n)}} + w_{ij}\left[ax + by + g^{(n)}\,\Delta z/2\right]\right\} \\ 2w_{ij}^2 a g^{(n-1)} \\ 2w_{ij}^2 a g^{(n)} \\ 0 \\ 0 \end{pmatrix},$$

and (A-5)

$$\begin{pmatrix} \partial s_{ij}^{(1)}\big/\partial y \\ \partial s_{ij}^{(2)}\big/\partial y \\ \partial s_{ij}^{(3)}\big/\partial y \\ \partial s_{ij}^{(4)}\big/\partial y \\ \partial s_{ij}^{(5)}\big/\partial y \\ \partial s_{ij}^{(6)}\big/\partial y \end{pmatrix} = Z^{-1}\begin{pmatrix} 2w_{ij}b\left\{\sqrt{a_{ij}^{(n-1)}} + w_{ij}\left[ax + by + g^{(n-1)}\left(z^{(n-1)} - z^{(n-2)} - \Delta z/2\right)\right]\right\} \\ 2w_{ij}b\left\{\sqrt{a_{ij}^{(n)}} + w_{ij}\left[ax + by + g^{(n)}\,\Delta z/2\right]\right\} \\ 2w_{ij}^2 b g^{(n-1)} \\ 2w_{ij}^2 b g^{(n)} \\ 0 \\ 0 \end{pmatrix},$$

where

$$Z = \begin{pmatrix} z_1^5 & z_1^4 & z_1^3 & z_1^2 & z_1 & 1 \\ z_2^5 & z_2^4 & z_2^3 & z_2^2 & z_2 & 1 \\ 5z_1^4 & 4z_1^3 & 3z_1^2 & 2z_1 & 1 & 0 \\ 5z_2^4 & 4z_2^3 & 3z_2^2 & 2z_2 & 1 & 0 \\ 20z_1^3 & 12z_1^2 & 6z_1 & 2 & 0 & 0 \\ 20z_2^3 & 12z_2^2 & 6z_2 & 2 & 0 & 0 \end{pmatrix}.$$

VITA

Vincent Bernard Durussel

Educational background

2000-2002 IFP / Texas A&M University France / USA
Resevoir Geosciences & Engineering (joint program between IFP &TAMU)
- Master of Sciences in Geophysics (Texas A&M University)
- Master in Reservoir Engineering (French Petroleum Institute)

1995-1998 *Université Pierre & Marie Curie* Paris, France
- Engineer degree in Geosciences (*Institut des Sciences et Technologies*)

Professional experience

2002-? CGG Americas Houston, USA
- Processing Geophysicist in the Marine Department.

1998-2000 Halliburton Pointe-Noire, Congo
- Field Engineer in the Logging and Perforating Department.

1998-1998 Total EP Paris, France
- Research project (six months) on the use of mode-converted waves in seismic exploration.

1997-1997 Elf EP Pau, France
- Internship (two months and a half) in the Laboratory of Rock Mechanics.

Permanent address

21, place Van Gogh,
95400 Villiers-le-Bel
France.
(33) 1 34 19 81 68
v_durussel@hotmail.com